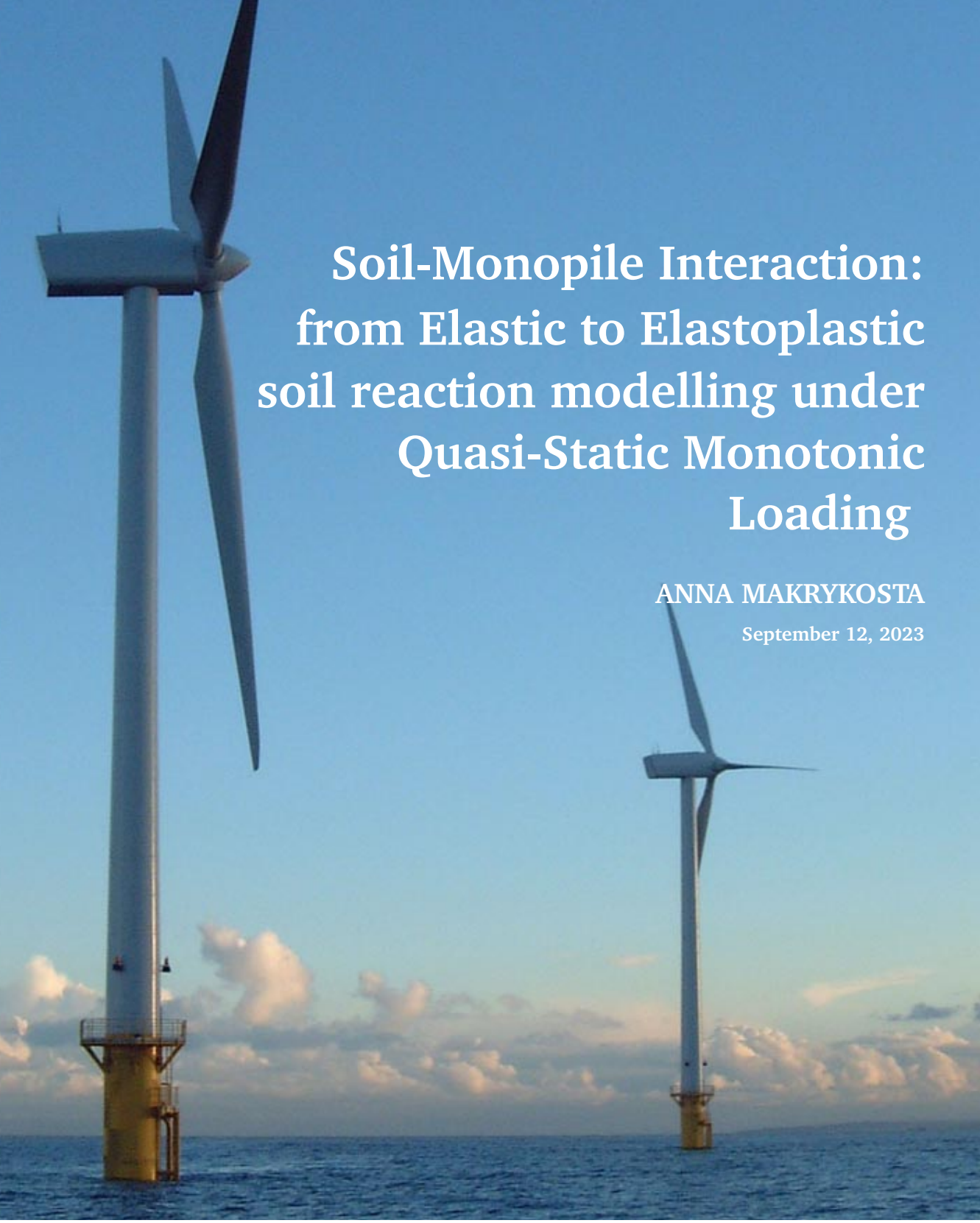

Soil-Monopile Interaction: from Elastic to Elastoplastic soil reaction modelling under Quasi-Static Monotonic Loading

ANNA MAKRYKOSTA

September 12, 2023

TU Delft Delft University of Technology

SIEMENS Gamesa RENEWABLE ENERGY

Soil-Monopile Interaction: from Elastic to Elastoplastic soil reaction modelling under Quasi-Static Monotonic Loading

Master of Science Thesis

Author:	Anna Makrykosta	(St. Number: 5600294)
Committee:	Dr. Ir. Federico Pisanò	TU Delft - Chairman
	Dr. Ir. Apostolos Tsouvalas	TU Delft
	Dr. Ir. Evangelos Kementzetzidis	TU Delft
	Ir. Stavros Panagoulias	TU Delft - SGRE

Cover: Offshore windfarm at Blyth, Northumberland, UK. (Image courtesy of AMEC.)

An electronic version of this thesis is available at http://repository.tudelft.nl/.

September 12, 2023

TU Delft Delft University of Technology

SIEMENS Gamesa RENEWABLE ENERGY

«Θαρσεῖν χρή, τάχ᾽ αὔριον ἔσσετ᾽ ἄμεινον»

[Take heart, tomorrow things may be better.]

Theocritus, 3rdC BC, Ancient Greek Poet.

Abstract

Offshore wind energy's rapid expansion underscores the need for accurate and efficient methods to analyze the behavior of monopile foundations supporting wind turbines. While three-dimensional (3D) analyses provide comprehensive insights, their computational demands are significant. As an alternative, one-dimensional (1D) models with spring elements to simulate the interaction between the structure and the surrounding soil, offer efficiency and simplicity. Realistic soil behavior, characterized by elastoplasticity, necessitates proper calibration of the spring models in 1D analysis.

This thesis addresses the challenge of soil-monopile interaction analysis, specifically focusing on the monopile response under lateral static monotonic loading. The research commences by highlighting the development imperatives in monopile-founded offshore wind turbines. The first phase involves calibrating elastic springs through a comprehensive review of existing literature. This calibration accounts for variations in spring stiffness along the monopile's length. Subsequently, the study progresses to elastoplastic soil modelling, adopting a linear elastic perfectly plastic approach and employing only lateral shaft springs. Acknowledging the limitations of linear elastic perfectly plastic *p-y* response, new material models, namely a bilinear and an exponential model, are examined. A parametric analysis encompassing various monopile geometries and lateral load eccentricities is conducted. An optimization routine refines the bilinear and exponential model parameters to closely match 3D responses. The results demonstrate satisfactory agreement for the analyzed high L/D monopiles, yielding valuable insights and conclusions. However, the low L/D monopiles exhibit a less successful match, primarily attributed to the absence of rotational shaft springs in the analysis.

Furthermore, empirical design processes for applying the bilinear and exponential models are outlined. These processes are founded on the relationships be-

tween the model parameters and the length-to-diameter (L/D) ratio as well as the eccentricity-to-diameter (e/D) ratio. The study highlights the applicability of the bilinear model across various soil conditions, monopile geometries and lateral load eccentricities. In contrast, the exponential model's efficacy is constrained by the examined L/D ratios, warranting further analyses for expanded application.

In conclusion, this thesis presents a systematic transition from elastic to elasto-plastic modelling for soil-monopile interaction analysis under static monotonic loading. The proposed bilinear and exponential models enhance the accuracy of 1D simulations, facilitating efficient design and analysis of monopile-founded offshore wind turbines. These methodologies contribute to the advancement of sustainable offshore wind energy, catering to diverse soil conditions and design scenarios.

Acknowledgements

As I conclude this Master's Thesis, I'm excited to complete my postgraduate studies at TU Delft's Faculty of Civil Engineering. This transformative two-year journey through the Geo-Engineering master's track has reached its destination, offering invaluable insights in geotechnical engineering that will shape my future pursuits.

I express my sincere gratitude to my supervisors Federico Pisanò, Apostolos Tsouvalas, Vagelis Kementzetzidis, and Stavros Panagoulias for their unwavering guidance and scientific support throughout this journey. I'm particularly thankful to Federico and Apostolos for infusing fresh perspectives into the project, and to Vagelis and Stavros for their continuous insights that have shaped the evolution of this master's thesis. Their mentorship has provided me with a profound understanding of offshore geotechnics research and the means to overcome academic challenges.

I also want to express my appreciation to Sachin, Stavros, and my fellow SGRE students for our bi-weekly meetings, fostering a shared journey through challenges and triumphs. Additionally, I extend my gratitude to Dimitra Delavinia, whose pioneering work laid the foundation for my own research.

Lastly, my heartfelt gratitude goes to my family and close friends, unwavering pillars of support, providing strength and encouragement through both joyful and challenging times. In particular, I want to honor the memory of my beloved father, whose guidance and inspiration continue to shape my journey, even in his absence. Your enduring love and unity have been a beacon of light guiding me forward.

Warmly,
Anna Makrykosta
Delft, September 2023

Contents

List of Figures

List of Tables

Nomenclature

Latin symbols

D	Diameter	m
E	Young's modulus	kPa
F, H	Lateral force	kN
G	Shear modulus	kPa
I	Second moment of inertia	m^4
K	Spring stiffness coefficient	$-$
K_r	Relative pile stiffness	$-$
L	Length	m
M	Moment	kNm
c	Cohesion	kPa
dz	Pile Element discretisation	m
e, h	Lateral load eccentricity	m
f	Yield function	kPa
k	Spring stiffness	kPa, kN/m
m	SL model parameter	$-$
p	Lateral reaction force	kN/m
q	Deviatoric stress	kPa
t	Pile thickness	m
u, y	Lateral deflection	m

Greek symbols

α	SL model parameter	$-$
γ	Shear strain	$-$
δ	Displacement	m
ϵ	Deformation	$-$
ζ_b	Ratio $F_{applied}/F_{max}$	$-$
θ	Rotation	rad
λ	Slenderness ratio	$1/m$
ν	Poisson's ratio	$-$
τ	Shear stress	kPa

Subscripts

el	Elastic
f	Failure
h	Hardening
$m-\theta$	Moment-rotation
max	Maximum
$p-y$	Lateral bearing pressure-deflection
$pile$	Pile property
q	Deviatoric
r	Reference
$soil$	Soil property
ult	Ultimate
y	Yield

Superscripts

B	Base
S	Shaft

Abbreviations

1D	One-Dimensional

3D	Three-Dimensional
BL	Bilinear
E	Elastic
EPP	Elastic Perfectly Plastic
FE	Finite Element
FEM	Finite Element Model
OWT	Offshore Wind Turbine
PL	Monopile
RBFOpt	Radial Basis Function Optimization
rMBE	relative Mean Bias Error
SL	Suryasentana and Lehane
ULS	Ultimate Limit State

Chapter 1

Introduction

1.1 Motivation

In the pursuit of achieving net-zero emissions, as outlined in DNV's energy transition outlook for 2022 [14], wind generated electricity is projected to grow five-fold by 2050, accounting for 29% of power generation compared to the modest 6% share in 2020. The limitations of land availability and community opposition will drive investment in offshore wind, even in regions that have not yet ventured into wind power. These regions include South East Asia and the Pacific area, which are highly prone to earthquakes. The significant increase in grid-connected wind electricity generation is depicted in Figure 1.1 (left), while the remarkable growth in fixed offshore wind installations is shown in Figure 1.1 (right).

Fixed offshore wind constitutes the largest share of offshore wind, with monopile being the most popular solution for founding an Offshore Wind Turbine (OWT) [36]. Monopile foundation holds the largest market share as it offers design and manufacturing simplicity, adaptability, and robust structural behavior [27]. Consequently, a comprehensive analysis of the static and dynamic responses of offshore wind turbines founded on monopiles is of great importance.

1.2 Research Background

Undoubtedly, the most precise approach to design an offshore wind turbine (OWT) monopile foundation involves Three-Dimensional Finite Element analyses (3D FE).

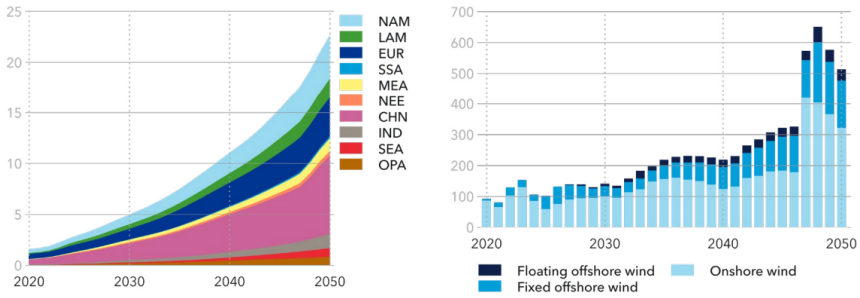

Figure 1.1: Grid-connected wind electricity generation by region, Units: PWh/yr (left) & Wind gross capacity additions, Units: GW/yr (right) [14].

However, these analyses come with considerable computational costs in terms of both time and complexity. Consequently, there is a growing academic interest in the exploration of more efficient alternatives, such as One-Dimensional Finite Element models (1D FEM). These models offer a simplified and efficient approach. They encompass the soil-monopile interaction utilizing the Beam-on-Winkler-Foundation approach, employing discrete springs to represent soil lateral loads.

Over time, researchers have identified limitations in relying solely on lateral shaft springs for modelling the low L/D (length to diameter ratio) monopiles used in the offshore industry. As a result, these models have progressively incorporated additional soil reaction mechanisms to more accurately capture the response. These enhancements encompass the integration of base springs as well as rotational shaft springs, as depicted in Figure 1.2. The inclusion of base springs in the model is crucial because it accounts for the shear resistance at the pile tip, which arises from the substantial diameter of the pile and exerts a significant influence on the monopile's response. Furthermore, the incorporation of rotational shaft springs is essential for capturing the distributed moment generated by the shear stresses developed at the perimeter of the pile. These stresses arise from the rotation of the low L/D monopiles when subjected to lateral loading.

The seismic interaction of an OWT in the presence of a single-phased, linear viscoelastic soil layer has been previously investigated in Delavinia's master thesis [10]. The current master thesis draws insights from the recommendations outlined in [10], particularly concerning the alignment between 3D and 1D models within the linear regime. Subsequently, this investigation expands to encompass scenarios

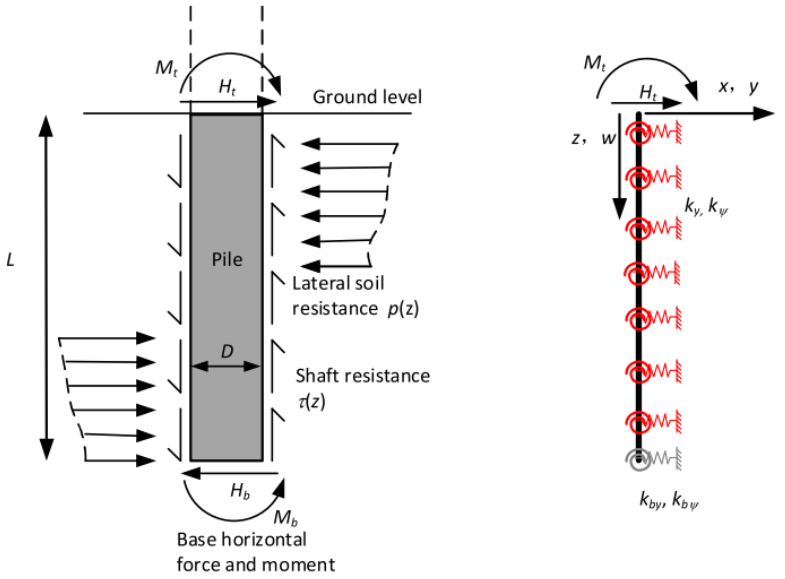

Figure 1.2: Soil resistance components acting on the monopile (left) & Four-spring beam model (right) [37].

involving a non-linear elastoplastic soil layer.

1.2.1 Variation of Spring Stiffness with Depth

In the studies conducted by Delavinia [10, 11], a disparity between the 3D and 1D finite element modelling of the dynamic interaction and seismic response of the soil-monopile-superstructure system is reported. The analysis incorporates both translational and rotational springs, characterized by uniform stiffness values along the length of the pile. The calibration of these springs involves subjecting the system to a static monotonic lateral load and moment at the monopile head for translational and rotational springs, respectively. The calibration process entails manual adjustment to achieve the best alignment between the 3D and 1D results. The alignment is established either by matching the average response over depth or by focusing solely on the response at the monopile head.

Considering the ultimate objective of evaluating the seismic interaction of the

soil-monopile-superstructure system, it is pertinent to question why the spring stiffness is calibrated based solely on static soil-monopile interaction. In line with the findings of Anoyatis et al. [2], who examined the kinematic response of piles embedded in a homogeneous soil layer, their findings reveal that the soil reactions demonstrate a weak frequency dependency. This is more pronounced for frequencies below the 'cutoff' frequency, which represents the threshold below which no radiation damping is generated. Consequently, the stiffness coefficient calibrated under static conditions can be reliably employed in dynamic analyses.

The discrepancy between the 3D results and the 1D prediction becomes apparent when examining the moment and deflection profiles of both slender and rigid monopiles. To improve the prediction of these profiles, it is recommended to consider spring stiffness values that vary with depth [10]. Some researchers have already investigated the variation of spring stiffness with depth. In order to provide results and tools that can be readily adopted and utilised by the industry, this work will only present the most relevant and applicable findings from the research community.

PISA design model [7]

The *PISA design model*, introduced by Burd et al. [7], provides a design approach for monopiles embedded in homogeneous sand sites. This model is applicable to monopiles with geometries in the range of 5m $\leq$ D $\leq$ 10m and 2 $\leq$ L/D $\leq$ 6, as well as lateral load eccentricities in the range of 5 $\leq$ h/D $\leq$ 15. According to the model, the *p-y* curves are defined for the case of monotonic lateral load. The *PISA design model* considers four separate components of soil reactions: distributed load p and distributed moment m acting along the pile, and lateral force H_B and moment M_B acting on the base of the pile. For each one of the four soil reaction components, a four parameter conic function is employed. These parameters include the ultimate displacement or rotation, the ultimate soil reaction, the initial stiffness, and the curvature. By varying the curvature parameter between the extreme values of 0 and 1, the conic function can adopt a bilinear form, as illustrated in Figure 1.3

The *PISA design model* is specifically formulated to simulate soil-monopile reactions from low deformations up to geotechnical failure. Hence, it can be used to simulate the case of linear elastic soil model by considering only the initial stiffness. The initial stiffness is found to be linearly dependent on the sand's relative density and the depth-to-diameter ratio. Notably, the stiffness decreases from the surface to the pile tip. A first degree function has been defined for the initial spring stiffness

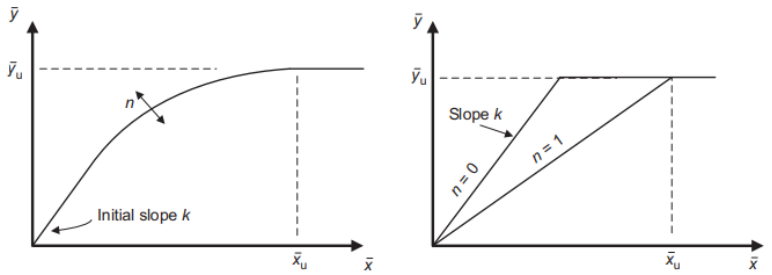

Figure 1.3: Utilizing a four-parameter conic function to model soil reaction component : Conic form (left) & Bilinear form (right) [7] - Notation: y in the Figure refers to the soil reaction, x refers to the displacement or rotation and n to the curvature.

k_p, for the case of 75% relative density. Therefore, by substituting the depth-to-diameter ratio, the initial spring stiffness over the depth of the monopile can be accurately computed.

Proposed relationships by Wan et al. [34]

The applicability of the *PISA design model* is challenged when dealing with different soil types, necessitating calibration. Recognizing this complexity, Wan et al. [34] proposed a more versatile approach for determining the initial lateral and rotational spring constants. Their study focuses on monopiles with a range of $2 \leq$ L/D ≤ 8 and lateral load eccentricities of $2 \leq$ h/D ≤ 16, considering linear elastic soil behavior and a perfectly rigid pile response.

Initially, the case of a homogeneous soil was examined, by conducting multiple 3D FE analyses. Based on the outcomes of these analyses, dimensionless stiffness coefficients were deduced for both linear *p-y* and *m-*θ shaft springs, as well as for the base springs. Notably, these derived coefficients exhibited variations dependent on depth, influenced by lateral load eccentricity and the length-to-diameter ratio of the monopile. To validate the results obtained from the 3D FE analyses, conventional beam column analyses were executed, where the derived stiffness values were input. Notably, both the 3D FE simulations and the beam column analyses, the latter representing, in essence, 1D evaluations, yielded consistent results. Despite this alignment, challenges arose in directly applying the resultant depth-dependent dimensionless stiffness coefficients to practical engineering scenarios. As a result,

the focus shifted towards identifying shaft stiffness coefficients that remain depth-independent, while accurately capture the monopile response. This pursuit involved a gradual simplification of spring components, evaluating their individual significance throughout the process. The findings reveal that the incorporation of both shaft rotational springs and base lateral and rotational springs significantly leads to a significant improvement in predicting the monopile's response. Notably, as the stiffness terms are simplified or omitted, the accuracy of the beam column model diminishes accordingly.

Moreover, this study delved into the application of the dimensionless stiffness coefficients within the context of a non-homogeneous soil scenario. For this investigation, the scenario encompassing all four spring reaction components was taken into account, referred to as *Case 1*. This was the most detailed case considered, incorporating depth-independent spring coefficients. Surprisingly, this approach yielded a relatively good match, which is promising considering the limitations of the *PISA* functions in capturing the initial stiffness of non-homogeneous soils. Ultimately, the study concludes that the accuracy of the *Case 1* transfer functions holds true for monopiles with L/D $\geq$ 3, regardless of whether the soil exhibits homogeneity or non-homogeneity.

1.2.2 From Elasticity to Plasticity

After conducting the analyses and assessing the alignment under the assumption of linear elastic soil behavior, the investigation now progresses to include the plastic response of the soil. This shift focuses on implementing soil plasticity theories and exploring the non-linear behavior of the soil layer, specifically in relation to pile behavior. Furthermore, this transition to elastoplastic soil modelling brings the analysis closer to real soil behavior, which is inherently non-linear. This transition to soil plasticity is an intriguing research topic proposed by [10], who recommended the investigation of a non-uniform, non-linear, elastoplastic soil layer. Incorporating this recommendation adds further depth and significance to the study, as it addresses the complexities of real soil behavior in practical scenarios.

To accomplish this, the first step involves examining the response incorporating plastic soil modelling under static conditions. Additionally, to simplify the analysis and examine the fundamental aspects of the problem, the soil is assumed to be uniform. These methodological simplifications allow a focused investigation of the plastic soil response, laying the foundation and paving the path towards achieving the desired goal of analysing an OWT founded in a elastoplastic soil layer under and

subjected to seismic loading.

Transitioning into soil modelling within the framework of soil plasticity, it becomes crucial to establish the model setup for investigating soil-pile-structure interaction. This involves temporarily setting aside the consideration on the most suitable constitutive law for describing soil behavior. The model setup, introduced by Wang et al. [35], forms the basis of the analysis framework.

The study by Wang et al. [35] investigated the non-linear seismic soil-pile-structure interaction, by adopting the dynamic beam on non-linear Winkler foundation (BNWF) approach. This proposed configuration incorporated viscous dashpots to account for energy dissipation via radiation damping, with dashpot coefficients derived for linear elastic conditions. The coefficient selection for the dashpot followed recommendations by Gazetas and Dobry [16]. The material response for sand, described by *p-y* curves, drew from recommendations by Reese et al. [26]. The study revealed that the arrangement of non-linear springs and linear viscous dashpots had a significant impact on the calculated response of non-linear systems. Notably, more realistic results were achieved when the linear viscous dashpot was placed in parallel with only the linear component of the hysteretic element and in series with the hysteretic element, as depicted in Figure 1.4.

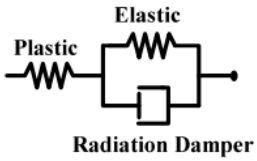

Figure 1.4: One-dimensional model setup for the dynamic BNWF approach, inspired by the initial concept presented by Wang et al. [35], and slightly modified by Rahmani et al. [24]

The study conducted by Wang et al. [35] revealed a crucial finding regarding the improved modelling of soil-pile-structure dynamic interaction by separating the soil into near field and far field zones. This division is based on the observation that the near field response exhibits significant soil non-linearity, while the far field response is predominantly characterized by elastic wave radiation. Both zones contribute differently to the overall system response. This necessity to analyze the interaction in two distinct steps is further supported by the work of Rahmani et al. [25], emphasizing the importance of considering soil layer deformation under seis-

mic excitation to accurately capture dynamic soil-pile interaction. In conclusion, the BNWF method demonstrated promise as a design tool for seismic soil-pile-structure interaction problems.

The pioneering approach introduced by Wang et al. [35] has been further advanced by numerous researchers to enhance the simulation of soil-pile interaction using sophisticated 1D model setups. Notably, Boulanger et al. [6] expanded upon the earlier model by incorporating a gap element in series. This addition enabled the simulation of inverted S-shaped *p-y* curves, capturing the influence of a physical gap and/or the undrained hysteretic behavior of the soil. In a subsequent study, Rahmani et al. [24] evaluated the effectiveness of the models proposed by Wang et al. [35] and Boulanger et al. [6] in predicting the behavior of piles subjected to seismic loading. The findings revealed that these models were inadequate as they failed to account for the degradation of soil stiffness during seismic events. As a result, numerous alternative approaches have been developed to more accurately capture the dynamic interaction between piles and soil.

Then, Kementzetzidis et al. [21], introduced a *p-y* model to analyze piles embedded in sandy soil and subjected to lateral cyclic loading. This new model incorporated memory-enhancement, addressing the soil ratcheting phenomenon that occurs during prolonged cyclic loading. Additionally, it incorporated elements to simulate the effects of pile-soil gapping. The proposed model consists of four springs: the memory-enhanced spring, the separation spring, the drag spring, and the closure spring. These springs are arranged in pairs to form the soil and gap elements, respectively. Figure 1.5 illustrates the proposed *p-y* model, showcasing a multi-component soil reaction scheme employed on each side of the pile. This is essential to account for the independent evolution of the gap during cyclic loading.

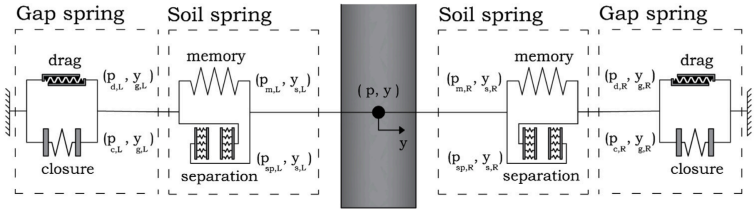

Figure 1.5: The *p-y* model configuration proposed by Kementzetzidis et al. [21].

The memory spring captures soil ratcheting, while the separation spring repre-

sents the separation of pile and soil during gapping. The drag spring simulates the frictional resistance generated by the soil against the pile during detachment, and the closure spring accounts for the inverted S-shaped stress-strain response cycles. In summary, the proposed model is an effective tool for analyzing piles subjected to lateral cyclic loading, providing a comprehensive understanding of their behavior in such conditions. However, it should be noted that the model's adequacy in capturing soil-pile behavior under seismic loading remains to be investigated.

1.3 Thesis Objective

The present master thesis builds upon the foundation laid by the previous study [10], aiming to refine its assumptions through a more realistic modelling approach. Specifically, the focus centers on the analysis of low L/D monopiles, a ratio that characterizes the rigid behavior of monopiles commonly employed for offshore wind turbine foundations. This characterization finds validation in several comprehensive investigations [30, 7, 34, 9]. Additionally, the analysis takes into account the lateral load eccentricity, as highlighted in the literature [7, 34]. By incorporating these changes, the resulting structural response closely reflects real-world conditions, making it applicable to industry practices.

The initial step involves validating the elastic spring calibration established by Delavinia [10] through a comparison with the analytical relationships presented by Hetényi [19]. Subsequently, the calibration of elastic springs follows the recommendations outlined by Wan et al. [34], with a subsequent comparison against the findings of [10]. The adoption of Wan et al.'s study [34] is justified by its applicability to soils with varying material properties and its potential for future use in non-homogeneous soil scenarios. Initially, the analysis involves only lateral translational springs, providing insight into the resulting response. The incremental inclusion of supplementary spring terms, as suggested by existing literature [7, 34], is systematically assessed. This stepwise evaluation aims to refine the soil-monopile-superstructure system's response to achieve the desired outcome. Ultimately, the primary objective is to evaluate the system's elastic response, which encompasses the calibration of elastic spring stiffness. This calibrated stiffness data is also proven valuable for the subsequent elastoplastic analyses.

Following this, the analysis shifts towards non-linear elastoplastic soil modelling. To enable the quantification of any potential discrepancies between the 1D and 3D response, this thesis focuses on conducting the analyses under static conditions. The

soil is modeled as an elastic-perfectly plastic material — a simplified yet commonly utilized approach in engineering practice. The calibration of the elastic spring is carried out based on the results obtained in the preceding step, while the examination of the plastic spring calibration follows. As the process advances, the model grows in complexity. The overarching goal, though not addressed in the current thesis, is to employ the cyclic *p-y* model introduced by Kementzetzidis et al. [21] for analyzing responses under cyclic loading. This lays the groundwork for the ultimate phase of analysis—the seismic examination of the soil-monopile-superstructure system.

1.4 Thesis Outline

In accordance with the thesis objective outlined earlier, the structure of the thesis is arranged as follows:

Chapter 2 *(Elastic Analyses)* validates the deduced 1D pile response through comparison with analytical solutions, and assesses the individual contributions of various spring components to this response. The ultimate objective is to accurately calibrate the elastic spring utilized in the 1D spring model setup.

Chapter 3 *(Elastoplastic Analyses)* encompasses the calibration of the elastoplastic material employed in the 3D analyses and explores diverse material models utilized in the 1D analyses, all with the aim of achieving optimal alignment under static monotonic loading.

Chapter 4 *(Conclusions & Recommendations)* provides a concise overview of the study's outcomes and offers suggestions for potential areas of future research.

Chapter 2

Elastic Analyses

2.1 Monopile and Soil Characteristics

First objective of this study is to evaluate the elastic response of the soil-monopile-superstructure system. The first step involves validating the 1D model's predictions against available analytical solutions. Subsequently, the lateral and rotational load transfer stiffnesses proposed by Wan et al. [34] will be gradually incorporated to examine their influence on the monopile's 1D response. Therefore, the selection of the pile-superstructure system will adhere to the geometric constraints specified in the aforementioned study, which are derived from industry practices as discussed in Section 1.3. Specifically, monopiles exhibiting semi-rigid behavior, with a relatively low L/D ratio, will be chosen.

However, categorizing monopiles as rigid or flexible based solely on their L/D ratio does not account for soil-monopile interaction [31]. Consequently, the pile bending stiffness relative to the soil is calculated and compared against threshold values advocated in existing literature [1] to determine whether the piles exhibit rigid, intermediate, or flexible behavior. The dimensionless pile relative stiffness, denoted as K_r, is defined by Equation 2.1. Values of K_r greater than 0.208 suggest a rigid behavior, while values below 0.0025 indicate a flexible pile response.

$$K_r = \frac{E_p I_p}{E_{soil} L^4} \tag{2.1}$$

In this study, a single thin-walled monopile (referred to as P3 in [10]) has been selected. The geometric characteristics of this pile are presented in Table 2.1, while the superstructure (referred to as S3), along with its properties, is described in Table 2.2. The soil properties utilized in the analysis are provided in Table 2.3.

Table 2.1: Pile characteristics for elastic analyses

Diameter D [m]	Length L [m]	L/D [-]	Wall thickness t [mm]	E_{pile} [GPa]	I_{pile} [m^4]	K_r [-]
7.5	36	4.8	75	210	12.06	0.0055

Table 2.2: Superstructure characteristics

Diameter D [m]	Length L [m]	Wall thickness t [mm]	E_{pile} [GPa]	Mass [Mg]
7.5	90	75	210	225

Table 2.3: Soil properties

Bulk Density [Mg/m^3]	Poisson's Ratio ν [-]	G_{soil} [MPa]	Strength τ_{max} [kPa]
1.84	0.30	106	100

2.2 Validation against Analytical Solutions

The validation of the 1D model involves comparing its results with the analytical solution presented by Hetényi in his study on elastically supported beams [19]. Hetényi's work primarily focuses on the analysis of beams supported by an elastic foundation, where the pressure at each point is directly proportional to the deflection of the beam at that point. This characteristic allows for the assumption that neighboring points' pressures and deflections have no influence on the response of the point being considered. Hence, the soil can be viewed as a collection of closely spaced *p-y* springs, exhibiting independent behavior.

While the loaded beam deflects, it is possible that in addition to the vertical reactions, there may also be some horizontal (frictional) forces along the surface where

the beam is in contact with the foundation. However, in Hetényi's work [19], the effect of such horizontal forces is not considered. The reaction forces on the foundation are assumed to be vertical at every cross-section. This assumption implicitly considers that transverse shear deformation is negligible and therefore, the angular distortion compared to the bending deformation of the entire beam is negligible as well. In other words, Hetényi applies the Euler-Bernoulli theory in his work [19].

Hetényi [19] derived the general solution for the differential equation governing the elastic line and obtained the mathematical equation for the deflection line under various boundary and loading conditions. In the case under consideration, the analytical solution assumes a beam with a finite length and a straight axis. It is important to clarify that in this context, the 'beam' refers to the monopile itself, which behaves as a beam with free ends (free head and free tip). The loading is applied at the head of the beam. The analytical solution is a function of the flexural rigidity of the monopile (EI_{pile}[kNm^2]) and the modulus of subgrade reaction(k[kN/m^2]).

2.2.1 Analysis of Pile Response: Zero and Non-Zero Eccentricity Cases

The analytical relationships proposed by Hetényi [19] are applied to the pile under examination, whose properties are listed in Table 2.1. Two different eccentricity ratios are considered and analyzed in this study. Firstly, the case of zero eccentricity, which was previously investigated in the study by Delavinia [10], is examined. The modulus of subgrade reaction for this case is determined based on the results of this current study. In the zero eccentricity case, the lateral load is applied at mudline level, resulting in no moment generation.

Next, the case of load eccentricity equal to four is evaluated. In this scenario, besides the lateral load, a moment is also imposed at the head of the pile. To analyze the pile's response, the superposition principle is adopted, which allows for the calculation of the combined effect of the 'Concentrated Force at one End' and the 'Concentrated Moment at one End' as described by Hetényi [19]. To determine the modulus of subgrade reaction in this case, the guidelines provided by Wan et al. [34] are followed. Specifically, the results from their study that focused on shaft lateral springs only are utilized, enabling a direct correlation between the analysis and their findings. A detailed examination of Wan et al.'s results is presented in the subsequent section.

For clarity, Table 2.4 summarizes the key characteristics of the loading conditions used in the analysis. The table also includes the calculated values of the flexural rigidity of the monopile (EI_{pile}[kNm^2]) and the modulus of subgrade reaction (k[kN/m^2]). These values are utilized to compute the slenderness ratio, given by $\lambda = \sqrt[4]{k/(4EI_{pile})}$.

Table 2.4: Analysis parameters

e/D [-]	k [kN/m^2]	EI_{pile} [kNm^2]	λ [1/m]	V [kN]	M [kNm]
0	794880	2532060782	0.9410	20000	0
4	826660	2532060782	0.0951	20000	600000

The validity of the 1D response is assessed by comparing the deflection and rotation profiles with the analytical relationship results, as depicted in Figure 2.1. In the 1D analysis, two different beam modelling approaches are employed. The first approach adopts the *elasticBeamColumn* modelling method for the beam elements, which incorporates the Euler-Bernoulli theory. This analysis directly aligns with the analysis conducted by Hetényi [19]. As observed from the graphs, the 1D results of this analysis exhibit identical deflection and rotation profiles to the analytical results, thus validating the 1D response.

The discretization of the pile in these analyses is set at 0.25m, which is consistent with the discretization employed in the work of [10]. A comparison with a more accurate discretization of 0.01m was made, and the deviation in the responses was found to be lower than 0.5% across the length of the pile, confirming the accuracy of the 0.25m discretization step.

In addition to the 1D results obtained using the Euler-Bernoulli theory, the 1D results based on the Timoshenko theory are also presented. The adoption of the Timoshenko theory is justified as it accurately models rigid monopiles. According to [18], the Euler-Bernoulli beam theory neglects the shear deformation, which can be significant in large-diameter piles but is accounted for by the Timoshenko beam theory. The necessity of employing *ElasticTimoshenkoBeam* elements to capture the shearing contributions to the rotations is also highlighted in the study by [33]. Their research demonstrated that including shearing effects was essential to achieve better agreement with the 3D response of monopiles supporting offshore wind turbines, which are characterized by their low slenderness ratio and rigid behavior.

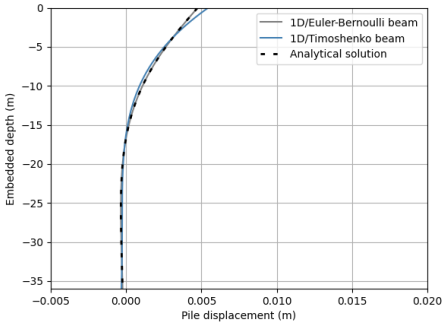

(a) Deflection profile - Zero eccentricity

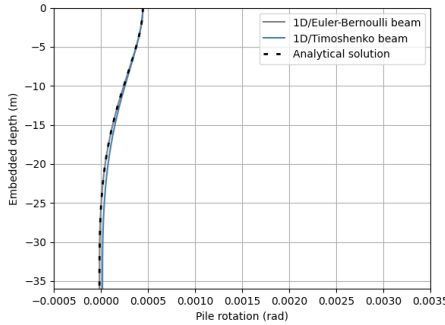

(b) Rotation profile - Zero eccentricity

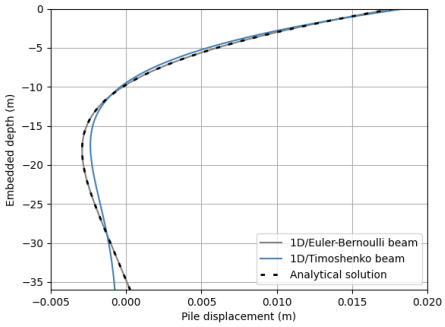

(c) Deflection profile - Eccentricity equal to 4

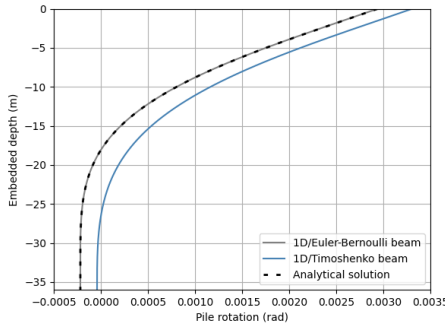

(d) Rotation profile - Eccentricity equal to 4

Figure 2.1: Deflection and rotation profiles along the length of the pile.

2.3 Adding up Soil Reaction Components

In previous analyses, only lateral translational springs were utilized. However, based on findings from Burd et al. [7] and Wan et al. [34], it has been highlighted that the low aspect ratio L/D and high eccentricity ratio e/D necessitate the inclusion of base and shaft m-θ springs to accurately capture the soil-monopile response. To evaluate and visually observe the altered response, a gradual inclusion of additional spring stiffness components is performed. The analysis begins with depth-independent spring stiffness values and implements the four cases as outlined in Wan et al.'s

study [34].

The examined monopile-superstructure system characteristics are listed in Tables 2.1 and 2.2. A static lateral load of 20MN is applied at an eccentricity of e/D = 4. The spring stiffness coefficients are calculated based on the guidelines provided in the study, considering the aspect ratio of the monopile under examination, which is equal to 4.80. These coefficients are logged in Table 2.5, beginning with the simplest scenario, referred to as *Case 4* and progressively advancing to the most intricate *Case 1*, where all the spring components are considered. The results from all four cases are detailed in Sections 2.3.1 and 2.3.2, while Section 2.3.4 provides the comparative conclusions.

Table 2.5: Spring stiffness coefficients for the four *Cases* as outlined in [34].

Case	K_{py}^{S} [-]	$K_{m\theta}^{S}$ [-]	K_{py}^{B} [-]	$K_{m\theta}^{B}$ [-]
4	7.80	-	-	-
3	6.83	-	2.65	0.79
2	6.37	1.00	2.65	0.79
1	4.34	6.70	2.65	0.79

It is worth noting that a previous investigation by [10] tackled the scenario where e/D = 0, which is not included in the work of [34]. In [10] study, dimensionless spring stiffness coefficients were manually fine-tuned, focusing solely on lateral translational springs. A subsequent comparison between the outcomes of [10] and those presented in [34] - *Case 4* is outlined in the following subsection. Later on, in Section 2.3.3, the case of adopting K_{py}^{S} & $K_{m\theta}^{S}$ dependent with depth is examined. The concluding remarks of this endeavour are presented in Section 2.3.4.

It is important to highlight that [34] study focused on analyzing a perfectly rigid pile. However, the current master thesis is devoted to depicting the genuine soil-monopile interaction, where the pile's behavior is not rigidly constrained. In particular, the analysed pile is classified as intermediate, based on its K_r value, indicated in Table 2.1. The distinction in modelling approaches may give rise to certain variations when contrasting the results derived form the two studies. Furthermore, the ultimate aim of the conducted elastic analyses resides in calibrating the elastic spring component employed within the elastoplastic analyses, a concept that will be elaborated upon in Chapter 3. The central objective here is to appraise the feasibility of calibrating these springs through the adoption of the proposed guidelines.

Lastly, to ensure the adequacy of spring density and mitigate inaccuracies arising from discretisation issues, a series of test analyses are conducted by varying the distance of the springs (dz). The analysis with dz=0.01m is regarded as the most accurate baseline, against which analyses with larger dz values are compared. It is observed that the rotation profile of the dz=0.25m analysis exhibits a maximum deviation of 5%. However, this deviation increases to approximately 10% in the case of dz=0.50m analysis.Considering a maximum acceptable error of 5%, a spring distance of 0.25m will be adopted for the subsequent 1D analyses. This choice aims to strike a balance between computational efficiency and accuracy in capturing the system's response.

2.3.1 Exclusive Lateral Shaft Springs Implementation

Case 4 represents the most straightforward scenario, characterized by the utilization of exclusively lateral *p-y* springs. The dimensionless spring stiffness coefficient for the specific pile under consideration is extracted from Fig. 9d [34], which is presented in Figure 2.2 for clarity. The displayed coefficient values are chosen to ensure a satisfactory stiffness match in the monopile head. By extracting data from the graph for L/D=4.80 and e/D=4, a specific value of K_{py}^{S}=7.80 is derived, as recorded in Table 2.5.

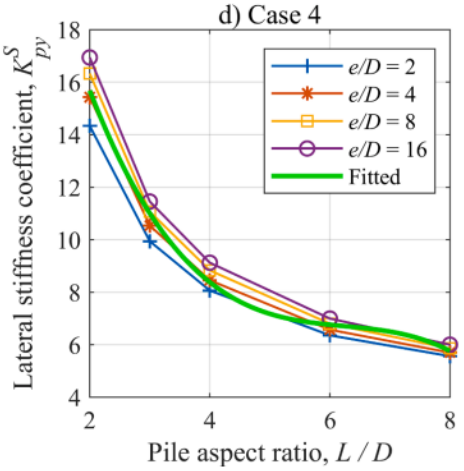

Figure 2.2: Shaft lateral stiffness coefficients for Case 4 - Fig. 9d [34].

Illustrated in Figure 2.2, a range of lateral load eccentricities spanning from 2 to 16 is subjected to examination. In her study, Delavinia [10] explores the scenario of zero eccentricity and establishes two distinct K_{py}^{S} values. The first value aims to align with the pile head deflection, while the second endeavors to match the average deflection over depth with the 3D FE results. To facilitate a meaningful comparison, the K_{py}^{S} value that aligns with the monopile head deflection is adopted. Delavinia's investigation yields a value of K_{py}^{S}=7.50 for P3S3 and e/D=0. Remarkably, this value closely approximates the one obtained from the graph in Figure 2.2 for the e/D=4 case. By extrapolating the apparent decreasing trend depicted in the graph, it is plausible to conceive that the e/D=0 case would have been positioned below the e/D=2 case, resulting in a value similar to that proposed by [10].

Furthermore, a computation of the spring stiffness coefficient based on the fitted line encompassing the entire load eccentricity range, as depicted in Figure 2.2, yields a value of K_{py}^{S}=7.37. This finding once again resonates with the manually calibrated value presented by [10]. This convergence is quite promising, suggesting that the outcomes from Wan et al.'s study [34] can potentially serve as a valuable reference for spring calibration, particularly in the context of *Case 4*. This holds true even though Wan et al.'s analysis centered on a perfectly rigid pile model.

Figure 2.3 illustrates the deflection and rotation profiles along the length of the monopile under a 20MN static monotonic load, applied at a distance of 30m from the mudline. As demonstrated, there is a generally favorable alignment observed throughout the pile's length. The deviation in monopile head stiffness, as utilized in Wan et al.'s study [34], is quantified by Equation 2.2.

$$Error = \left| \frac{K_u^{3D} - K_u^{1D}}{K_u^{3D}} \right| + \left| \frac{K_\theta^{3D} - K_\theta^{1D}}{K_\theta^{3D}} \right| \tag{2.2}$$

Upon employing the aforementioned error formula, the discrepancy in terms of translational stiffness at the monopile head amounts to approximately 17%, while the variation in terms of rotational stiffness at the monopile head is approximately 20%. This results in a total error of approximately 37% at the monopile head. When contrasting this error magnitude with the corresponding value depicted in Fig. 11d [34], which is estimated at around 17%, a noticeable disparity emerges. This discrepancy can be attributed to the fact that Wan et al.'s analysis considers a perfectly rigid pile, an assumption that markedly influences the outcome.

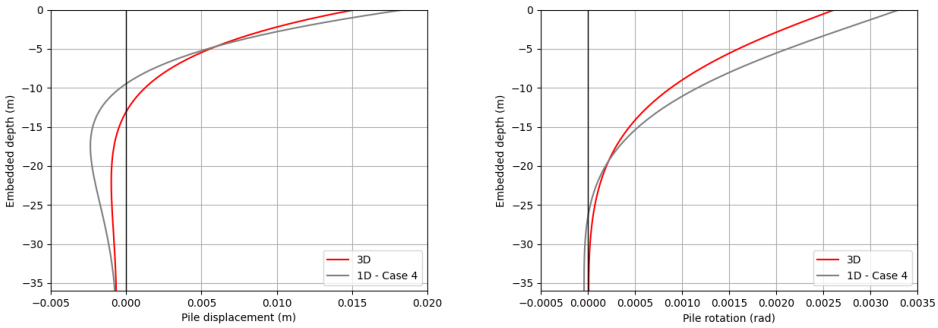

(a) Deflection profile

(b) Rotation profile

Figure 2.3: Deflection and rotation profiles along the length of the pile, comparing 3D and 1D-Case 4 from [34].

Indeed, in an endeavor to validate the error values stipulated in Wan et al.'s study [34], an exercise was undertaken to model a pile with a stiffness four orders of magnitude greater. Subsequently, the error was recalculated, yielding a value of 24%, which notably converges closer to the error reported by Wan et al. It is reasonable to expect such alignment when simulating a perfectly rigid pile. Hence, it is clear that the error values in Wan et al.'s study cannot be directly compared to the results of these analyses. To improve this alignment, introducing additional soil reaction mechanisms is necessary to determine if a more precise match can be attained.

2.3.2 Inclusion of Rotational Shaft Springs and Base Springs

Case 3

The absence of base springs is often considered a primary drawback of traditional *p-y* methods when applied to large diameter piles. Consequently, the initial step in incorporating additional soil reaction components involves introducing lateral and rotational base springs, a concept denoted as *Case 3* in the study by [34]. The dimensionless stiffness coefficients for these base springs, along with the lateral shaft coefficient extracted from Fig 6 & Fig. 9c of the mentioned study, are detailed in Table 2.5. The alignment of deflection and rotation profiles with respect to the 3D results is visualized in Figure 2.4.

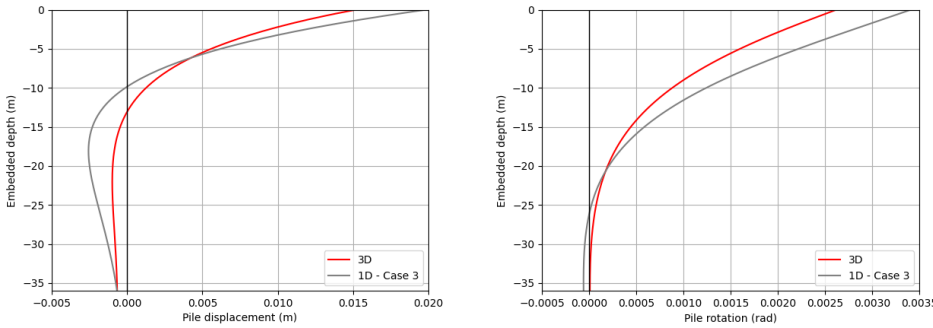

(a) Deflection profile **(b)** Rotation profile

Figure 2.4: Deflection and rotation profiles along the length of the pile, comparing 3D and 1D-Case 3 from [34].

The inclusion of base springs yielded a slight improvement in matching at the pile's tip. However, when considering the entire length of the pile and the monopile head, the alignment deteriorated in comparison to the previously examined *Case 4*. In quantitative terms, employing Equation 2.2, the error at the monopile head for *Case 3* is approximately 46%, whereas it was 37% for *Case 4*. This increased level of error can be attributed to the reduction of the dimensionless spring stiffness for the lateral shaft springs by 1.00, without compensating with an additional soil reaction component across the length of the pile. Consequently, it is reasonable to anticipate a softer response in the deflection and rotation profiles, which contributed to a further deterioration in the alignment.

Case 2

The subsequent phase involves incorporating shaft rotational springs. For *Case 2*, the non-dimensional moment coefficient is initially set to unity. As depicted in Fig. 5 of the study, the rotational stiffness coefficients obtained from 3D finite element analyses consistently approximate 1 across the entire length of the pile, for all examined load eccentricities and aspect ratios. This explains why this value was chosen. A notable observation arises from the coefficients recorded in Table 2.5 for the cases analyzed up to this point: the lateral shaft spring coefficient diminishes as more soil reaction mechanisms are integrated into the analyses. It's as if the stiffness previously provided by these springs is now being distributed among the other soil reac-

tion mechanisms. Considering that the rotational shaft spring stiffness is computed as a function of D^2, in contrast to the lateral shaft springs which are proportional to D, a substantial influence from the rotational shaft springs is anticipated. Figure 2.5 illustrates the match between the deflection and rotation profiles and the 3D results.

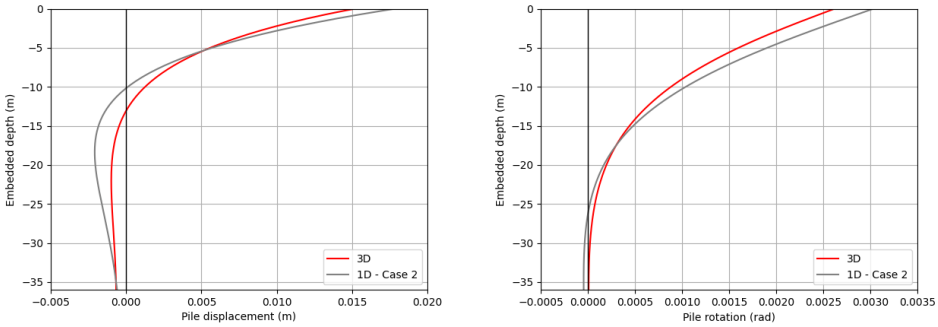

(a) Deflection profile **(b)** Rotation profile

Figure 2.5: Deflection and rotation profiles along the length of the pile, comparing 3D and 1D-Case 2 from [34].

In numerical terms, using Equation 2.2, the error at the monopile head for *Case 2* stands at approximately 27%, marking the least error observed among the examined cases. Notably, the alignment of the deflection and rotation profiles is significantly enhanced. As anticipated, both the local match at the monopile head and the alignment across the entire pile length are notably improved.

Case 1

The subsequent stage involves applying the optimized rotational shaft coefficient value recommended in Fig. 10 of the study. Upon examining the computed values listed in Table 2.5 for *Case 1*, it becomes apparent that a substantially higher rotational shaft coefficient is employed in this particular analysis. The outcomes of this analysis, pertaining to the distribution of deflection and rotation, are illustrated in Figure 2.6.

The utilization of a significantly higher rotational shaft coefficient resulted in an exceedingly rigid rotation profile, exhibiting a notable discrepancy at the rotation value of the monopile head. In contrast, the distribution of deflection along the

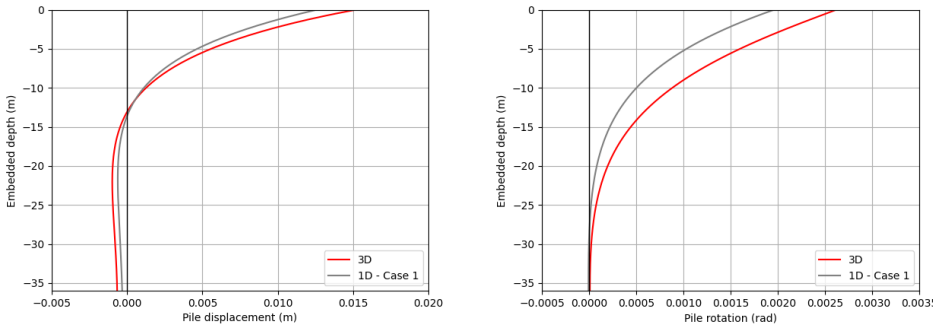

(a) Deflection profile

(b) Rotation profile

Figure 2.6: Deflection and rotation profiles along the length of the pile, comparing 3D and 1D-Case 1 from [34].

pile's length is the most favorable observed so far. However, locally at the monopile head, *Case 1* shows a larger disparity compared to *Case 2*. The pronounced deviation in both monopile head deflection and rotation values contributes to an error of approximately 54%, as computed using Equation 2.2. Consequently, among all the examined cases employing constant spring stiffness with depth, *Case 1* presents the poorest alignment in terms of monopile head stiffness.

2.3.3 Depth-Dependent Spring Stiffness

After evaluating the outcomes derived from the simplified scenarios featuring constant spring stiffness coefficients throughout the depth, there arises a necessity to investigate cases, where the spring stiffness varies along the length of the monopile.

Depth-Dependent Rotational Spring Stiffness

A straightforward adjustment involves introducing rotational spring stiffness that varies with depth. Given a lateral load eccentricity of 4, data is extracted from Fig. 5b of [34] study, depicted in Figure 2.7, showcasing the distribution of $K^S_{m\theta}$ across normalized depth. The graph presents outcomes for various aspect ratios, distinguished by different colors. The blue curve corresponds to L/D=4, while the green corresponds to L/D=6. In the case of L/D=4.8 under examination, an estimated distribution of $K^S_{m\theta}$ is derived.

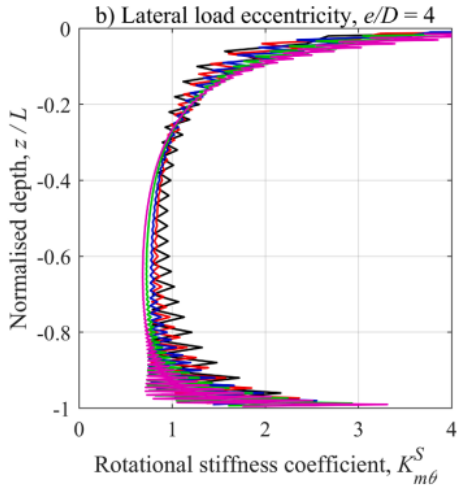

Figure 2.7: Rotational m-θ spring stiffness coefficient against normalised depth for e/D=4 - Fig. 5b [34].

Subsequently, a function that offers the best fit to the data is defined. Specifically, a sixth-order polynomial emerges as the optimal choice, closely aligning with the reported data points and achieving an R-squared value of 0.988. The employed $K^S_{m\theta}$ values span approximately 0.8 to 4, with a predominant concentration below 1.

To meaningfully assess the influence of varying spring stiffness with depth and conduct a comprehensive analysis, the remaining three spring coefficients are held constant throughout the depth, adopting the values utilized in *Case 2*. This selection is logical, considering that *Case 2* employs a uniform $K^S_{m\theta}$ value of 1 across the pile length. This new scenario is labeled as *Case 2 Modified*, and the outcomes of this analysis are illustrated in Figure 2.8.

Both the deflection and rotation profiles exhibit the most favorable alignment attained thus far, with the rotation profile demonstrating an exceptionally close fit. Furthermore, the match at the monopile head is notably enhanced. In terms of quantitative assessment, the error for the monopile head stiffness is calculated to be 7% using Equation 2.2. *Case 2 Modified* stands as the most successful achievement in terms of alignment, surpassing all previous matches.

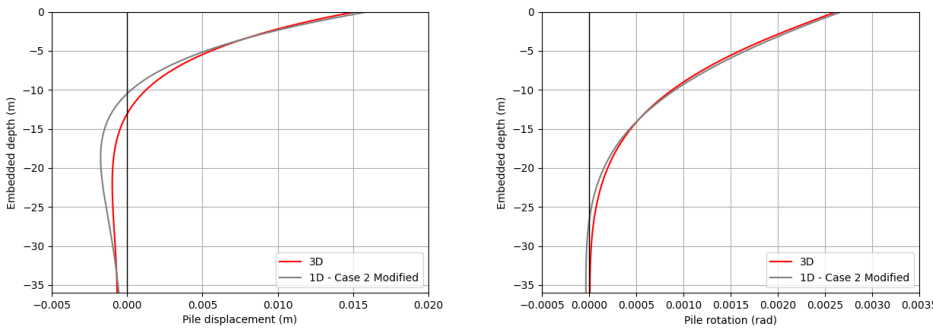

(a) Deflection profile

(b) Rotation profile

Figure 2.8: Deflection and rotation profiles along the length of the pile, comparing 3D and 1D-Case 2 Modified from [34].

Depth-Dependent Rotational & Lateral Spring Stiffness

To maintain analytical consistency, the integration of depth-dependent lateral spring stiffness is combined with rotational spring stiffness. The necessary data is extracted from Fig. 4b of [34], as illustrated in Figure 2.9. Importantly, the graphical representation underscores a noticeable stiffness discontinuity near the rotation point, and the overall curve shape exhibits complexities.

In an attempt to replicate the data extraction and function fitting technique, a decision was made to employ three distinct polynomials: one to represent the distribution above the rotation point and two for the curves below it. Upon conducting the analysis, a remarkable alignment was observed near the monopile head. However, in proximity to the rotation point, an anomalous deflection kick was noted. To address these observed discontinuities, an alternative approach was undertaken, involving the creation of a hypothetical distribution, as visualized in Figure 2.9.

This analysis produced deflection and rotation profiles similar to the case where only depth-dependent rotational spring stiffness was used (Figure 2.8). The deflection profile closely matches the 3D curve near the monopile head but shows slight differences in the lower part of the pile. Unfortunately, there is no significant improvement in the results. Additionally, this approach introduces uncertainties and practical challenges, making it less favorable for implementation.

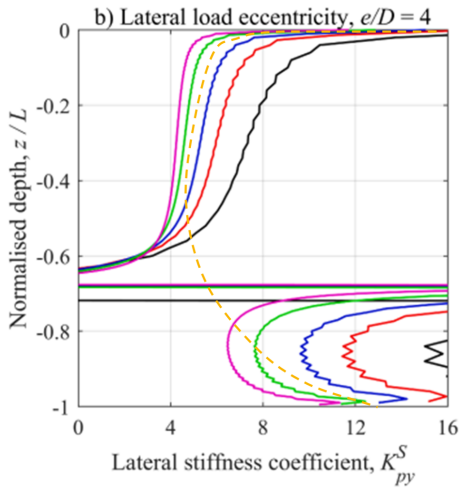

Figure 2.9: Lateral p-y spring stiffness coefficient against normalised depth for e/D=4 - Fig. 4b [34]. The dashed orange line on the graph illustrates the hypothetical distribution of K_{py}^{S} for L/D=4.8, as visually conceptualized by the author.

2.3.4 Concluding Remarks

After assessing the simplified scenarios utilizing constant spring stiffness with depth, referred to as *Cases 1-4* in the study by [34], several observations can be drawn.

Case 4, employing only lateral shaft springs, yields consistent and validated outcomes, as corroborated by the findings of [10].

Among the more intricate scenarios, *Case 3*, involving base springs, exhibits a slight improvement at the pile tip; however, the overall response deteriorates. In contrast, *Case 2* showcases a notably enhanced alignment in both the deflection and rotation profiles, as well as a superior match in monopile head stiffness. Remarkably, it achieves the most accurate rotation profile match compared to all other simplified cases.

Conversely, *Case 1* achieves the most accurate deflection profile, attributed to the utilization of a high $K_{m\theta}^{S}$ value. As elucidated in the study, the application of a constant K_{py}^{S} value along the monopile length results in significantly less reaction

to the applied moment, compared to the actual depth-dependent lateral spring stiffness distribution. To counterbalance this effect, an exceedingly large $K^S_{m\theta}$ value is employed for *Case 1*.

Overall, *Cases 1 & 2* exhibit notable deflection and rotation profiles, with the former excelling in deflection and the latter in rotation. In terms of lateral and rotational monopile head stiffness, *Case 2* attains the most favorable match.

For achieving even higher accuracy, *Case 2 Modified* yields remarkably favorable outcomes. Nevertheless, the implementation of depth-dependent spring coefficients poses challenges as each spring requires individual calibration. This complexity is further magnified when incorporating depth-dependent lateral and rotational springs, rendering this approach impractical for real-world application. The inclusion of depth-dependent spring coefficient analyses in the current master thesis serves to assess their impact; however, it is not recommended for practical use.

Finally, with the ultimate objective of eliminating the need for manual calibration, as performed in Delavinia's study [10], the focus is on finding a way to compute the elastic spring stiffness across varying L/D ratios and e/D conditions, primarily for the scenario where only lateral shaft springs are employed. As shown, *Case 4* [34] suggested parameters are proximate to the ones derived upon manual calibration [10] and their implementation yields satisfactory results. It is important to note that while the match between the 3D and 1D results is not the best among the examined cases, the simplicity of calibration and the inherent limitations of manual calibration methods make *Case 4* [34] a practical and advantageous choice. As a result, Figure 2.2 will be the primary reference for elastic spring calibration throughout this thesis.

Chapter 3

Elastoplastic Analyses

3.1 Initial Approach and Analysis Characteristics

In order to provide a more accurate representation of soil behavior, the current thesis aims to move beyond the analyses conducted solely in the elastic regime and delve into evaluating the elastoplastic response of the soil. This next step is crucial as it aligns with the reality of soil behavior, which is known to exhibit highly non-linear characteristics.

In line with common engineering practices, an initial and simplified approach to elastoplasticity involves assuming that the soil behaves as a linear elastic, perfectly plastic material. This is a simplified approach commonly adopted for its practicality, that may not fully capture the complex and non-linear behavior that is observed in soil. Despite its limitations, the linear elastic, perfectly plastic modelling of the soil serves as a valuable starting point for conducting elastoplastic analyses in the current research.

An extensive analysis was conducted on a set of piles, each sharing the same diameter and wall thickness but varying in length. The length of the monopiles examined ranged from 20m to 80m. The detailed characteristics of these piles are summarized in Table 3.1. The analyses were performed to evaluate the response of the piles under two different lateral load eccentricities, namely 8 and 4. These eccentricities were selected to represent realistic offshore loading scenarios. It is important to note that the focus was on static monotonic loading as already men-

tioned in Section 1.3 and the superstructure properties relevant to the study have been previously presented in Table 2.2.

Table 3.1: Pile characteristics for elastoplastic analyses

Notation	Diameter D [m]	Length L [m]	L/D [-]	Wall thickness t [mm]	E_{pile} [GPa]	I_{pile} [m^4]	K_r [-]
PL1	10.0	20	2.0	100	210	38.11	0.1815
PL2	10.0	30	3.0	100	210	38.11	0.0359
PL3	10.0	40	4.0	100	210	38.11	0.0113
PL4	10.0	60	6.0	100	210	38.11	0.0022
PL5	10.0	80	8.0	100	210	38.11	0.0007

When the symbol * is used after the regular notation of the piles, as presented in Table 3.1, it indicates that a lateral load eccentricity of 4 is applied in the analyses. Conversely, the plain notation corresponds to a load eccentricity of 8. For example:

$$PL4 \longrightarrow PL4 \text{ characteristics and } e/D = 8$$
$$PL4^* \longrightarrow PL4 \text{ characteristics and } e/D = 4$$

These notations are used to distinguish the two cases in the analyses.

3.2 3D FE modelling

To address the system's nonlinear response, 3D analyses are performed using the Finite Element (FE) software OpenSees. Exploiting the model's intrinsic symmetry, the FE mesh is divided along the $y = 0$ plane. Consequently, the cross-sectional properties of the pile, along with its stiffness and applied lateral static loads, are all reduced by half. In modeling the pile, 1D Timoshenko beam elements and horizontal rigid links are employed. These rigid links connect the embedded beam nodes to adjacent soil nodes, effectively representing the area occupied by the pile.

The lateral boundaries of the soil domain are placed at a distance of 25 times the diameter of the pile from the pile axis, and the depth of the domain extends approximately 1.8 times the pile diameter. Importantly, the FE mesh boundaries are positioned at a sufficient distance from the pile to minimize their influence on the pile's response, as detailed in [4]. Mesh discretisation is finer in close proximity to the pile and gradually coarsens towards the lateral boundaries, as visually depicted

in Figure 3.3. The number of elements required to represent the soil domain vary, ranging from approximately 4.700 for PL1 to around 18.000 for PL5. At the lateral boundaries of the model, a shear beam boundary condition is applied, where nodes at the same depth share identical lateral and vertical displacements, forming a 'tied-node' boundary condition. Additionally, vertical displacements at the bottom of the layer are fixed to simulate the presence of an underlying rigid bedrock.

The soil material model used in the 3D analyses is calibrated to exhibit a linear elastic, perfectly plastic behavior. The soil is modeled using *SSPbrick* elements (Stabilized Single Point), which are eight-node hexahedral elements with a single integration point. In this study, a uniform soil layer is considered, meaning that the soil is pressure independent. OpenSees library provides a material model specifically designed to describe the behavior of such soils, known as the *PressureIndependMultiYield* material. This material model is commonly used for clayey or organic soils loaded under undrained conditions. Plasticity is formulated based on the multi-yield-surface plasticity concept with an associative flow rule, and the yield surfaces are of the Von Mises type. A representation of the Von Mises multi-surface kinematic plasticity model is depicted in Figure 3.1.

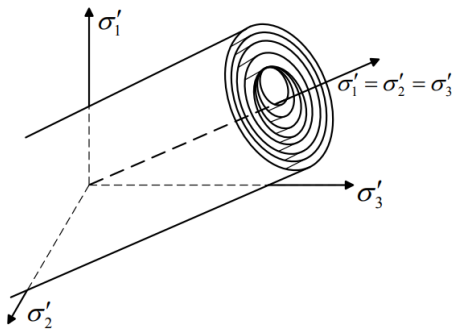

Figure 3.1: Von Mises multi-surface kinematic plasticity model. [22]

The non-linear shear behavior of the soil is represented using a shear stress-strain backbone curve in the material model (Figure 3.2 (left)). By default, the model utilizes 20 yield surfaces to define the backbone curve. These surfaces are generated based on the hyperbolic relation described in Equation 3.1, where τ represents the octahedral shear stress, γ denotes the octahedral shear strain and G_r is the low-

strain shear modulus. The parameter γ_r serves as the reference shear strain, while τ_f represents the peak shear strength and γ_{max} corresponds to the maximum shear strain. However, since the intention is to model an elastic perfectly plastic behavior for the soil, the number of yield surfaces is specifically set to 1. This choice ensures that the soil's response aligns with the desired elastic perfectly plastic behavior (Figure 3.2 (right)).

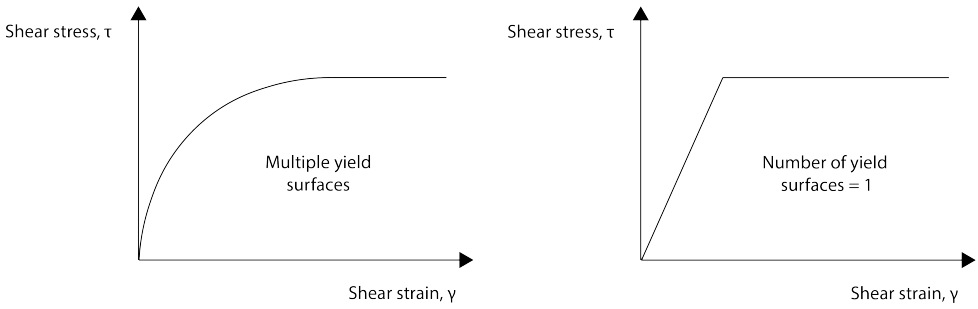

Figure 3.2: Soil backbone curve for multiple yield surfaces (left) and a unique yield surface (right).

$$\tau = \frac{G_r \gamma}{1 + \frac{\gamma}{\gamma_r}}, \quad \text{where} \quad \gamma_r = \frac{\tau_f \gamma_{max}}{G_r \gamma_{max} - \tau_f} \tag{3.1}$$

Lastly, the algorithm used in the finite element analysis is changed from the *Newton* algorithm to the *Krylov-Newton* algorithm. This choice is made because the *Krylov-Newton* algorithm object accelerates the convergence of the modified Newton method, making it preferable for the current elastoplastic analyses.

The implementation of the material model is assessed by evaluating its performance in multiple soil elements strategically positioned throughout the domain. Figure 3.3 depicts a typical FE mesh, highlighting the examined soil elements with different colors, along with the indication of the direction of the applied static loading. Specifically, two soil elements are considered: one located near the pile at a shallow depth and longitudinal distance (blue), and another situated at the rear in relation to the loading direction (red). Additionally, the analysis includes one soil element at the mudline level (black), two points near the lateral boundary (purple) and the depth boundary (green), as well as an intermediate point at an abstract location (cyan).

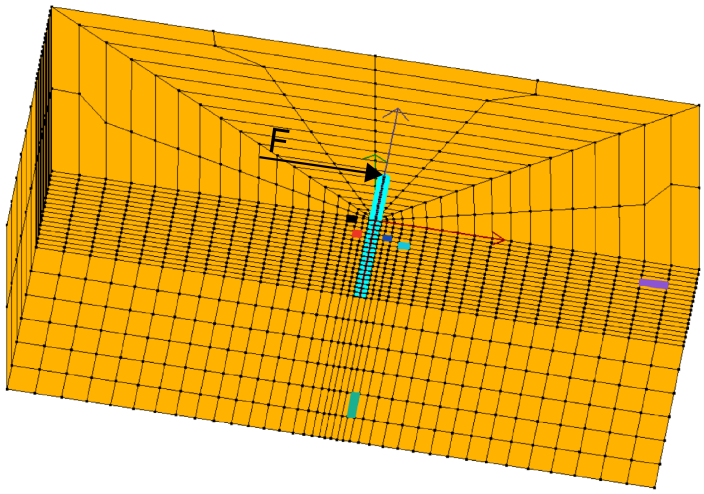

Figure 3.3: 3D FE mesh visualised via OpenSeesPL, showcasing the highlighted soil elements.

The *PressureIndependMultiYield* material model incorporates plasticity exclusively in the deviatoric stress-strain domain. To verify the accurate implementation of the soil material, the deviatoric stress-strain relationship is computed for the highlighted soil elements. Figure 3.4a presents the deviatoric stress-strain diagrams obtained through a static loading pushover analysis with a loading increment of 10kN over 1000 steps, resulting in a final load of 10MN. The equations governing the deviatoric stress and strain are given by Equation 3.2 and Equation 3.3, respectively.

$$q = \frac{1}{\sqrt{2}}\{[(\sigma_{xx} - \sigma_{yy})^2 + (\sigma_{yy} - \sigma_{zz})^2 + (\sigma_{zz} - \sigma_{xx})^2] + 6\tau_{xy}^2 + 6\tau_{yz}^2 + 6\tau_{zx}^2\}^{\frac{1}{2}} \quad (3.2)$$

$$\epsilon_q = \frac{\sqrt{2}}{3}\{[(\epsilon_{xx} - \epsilon_{yy})^2 + (\epsilon_{yy} - \epsilon_{zz})^2 + (\epsilon_{zz} - \epsilon_{xx})^2] + 6\gamma_{xy}^2 + 6\gamma_{yz}^2 + 6\gamma_{zx}^2\}^{\frac{1}{2}} \quad (3.3)$$

Based on the information provided in Figure 3.4a, it can be observed that all soil elements that enter the plastic zone reach a stress level of 200 kPa and maintain this stress level as the strain increases. This behavior indicates the correct implementation of elastic perfectly-plastic response. Furthermore, the maximum deviatoric

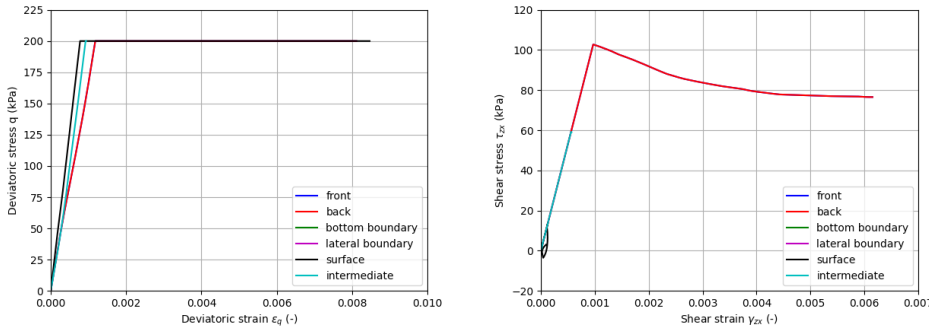

(a) Deviatoric stress-strain diagram.

(b) Shear stress-strain diagram.

Figure 3.4: Stress-strain diagrams under a static loading of 10MN, plotted for the soil elements corresponding to Figure 3.3.

stress amplitude is equal to 200 kPa. This signifies the magnitude of the stress difference between the principal stresses. The Von Mises yield function, denoted by f, can be described by Equation 3.4:

$$f = q - 2c \tag{3.4}$$

According to the stress paths of the soil elements entering the plastic region, it can be inferred that they lie on the yield contour where the Von Mises yield function, f, equals 0. By applying the Equation 3.4 and using a cohesion value of 100 kPa, which is the previously mentioned soil's strength τ_{max}, the stress parameter, q, can be defined. Substituting f = 0 and c = 100 kPa into the Equation 3.4:

$$f = 0 \xrightarrow{Eq.3.4} q - 2c = 0 \Rightarrow q = 2c \xrightarrow{c = 100kPa} q = 200kPa \tag{3.5}$$

Therefore, based on this analysis and substitution, the stress parameter associated with the deviatoric stress, q, is determined to be 200 kPa (Equation 3.5).

The two soil elements located at the same depth, with one in front and the other at the back of the pile in relation to the loading direction, exhibit an identical deviatoric stress-strain response (highlighted in blue and red, respectively). This similarity can be attributed to the absence of tension cutoff in the material model. Since no tension cutoff has been implemented, both soil elements experience the same behavior under tensile stresses. This results in their deviatoric stress-strain curves being

identical, as they respond in the same manner to increasing strain.

A simpler, yet significant check lies in determining the inclination of the τ-γ diagram. The ratio of the shear stress to shear strain should be equal to the shear modulus G, for all soil elements examined. Indeed, all stress paths presented in Figure 3.4b have the same slope, which is equal to $G = 105982kPa$.

3.3 1D modelling

To accommodate elastoplastic behavior, a calibration process is employed for the springs, utilized in simulating the soil-monopile interaction. Specifically, only *p-y* shaft springs are employed to ensure better control over the calibration of the 1D response. The elastic spring calibration is performed following the methodology established by Wan et al. [34] and presented in Section 2.3.1. The main challenge lies in calibrating the p-y response of the springs to align the results obtained from the 1D analysis with those from the 3D analysis. In essence, this involves determining the parameters that define the plastic spring response.

3.3.1 Scaling the Soil stress-strain Response

Researchers have proposed a mathematical approach, as outlined in two studies by Zhang et al. [38] and Jeanjean et al. [20], for generating the *p-y* spring response by scaling the shear stress-strain curve. This methodology focuses on clayey soil and is particularly applicable in the deeper sections of a pile, where the dominant failure mechanism under static monotonic loading conditions is deep (flow around) failure.

The essence of this approach involves scaling the measured shear stress-strain curve obtained from laboratory tests to accurately represent the behavior of the soil as a spring. The motivation behind this idea stems from the observation that the shape of the *p-y* curve exhibits similar characteristics to the soil stress-strain curve. In other words, the stiffness of the calculated *p-y* response is directly influenced by the stiffness of the soil stress-strain response, as discussed in Zhang et al. ([38]).

In the work of Zhang et al. [38], the scaling methodology introduces a relationship between mobilization in shear stress and lateral bearing pressure, assuming that the ratio of shear stress (τ) to its ultimate value (s_u) is equivalent to the ratio of lateral bearing pressure (p) to its ultimate value (p_u), i.e., $\frac{\tau}{s_u} = \frac{p}{p_u}$. This assumption forms the basis for their method to scale the normalized lateral displacement ($\frac{y}{D}$)

using shear strain. To facilitate scaling, the authors introduce two dimensionless scaling coefficients. The first coefficient, denoted as ξ_1, has a constant value of 2.8 and is used in the scaling procedure. The second coefficient, ξ_2, is dependent on the roughness of the pile (α). Specifically, ξ_2 is calculated as $\xi_2 = 1.35 + 0.25\alpha$. The overall scaling procedure is illustrated in Figure 3.5.

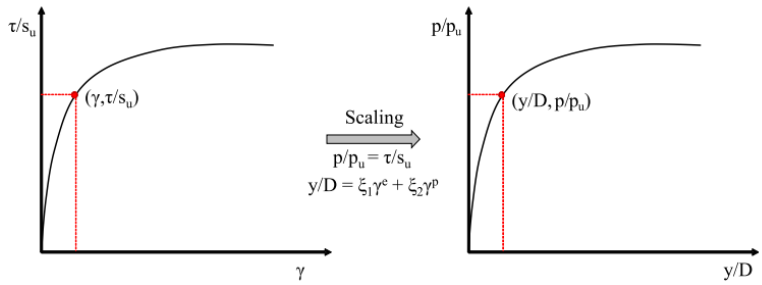

Figure 3.5: Schematic illustration of proposed scaling procedure, as presented in the study of Zhang et al.[38].

On the other hand, Jeanjean et al. [20] propose a different scaling methodology, where the level of lateral bearing pressure mobilisation is not assumed to be directly equivalent to the $\frac{\tau}{s_u}$ ratio. Instead, the following relationship is introduced:

$$\frac{p}{p_u} = \frac{\tanh(A\left(\frac{(y/D)p}{(y/D)pf}\right)^{0.5})}{\tanh(A)} \tag{3.6}$$

In this equation, A represents a parameter in the *p-y* curve model, which is calculated as $A = 1.33 + 0.45\alpha$, where α is the stress-strain curve parameter. This relationship demonstrates a correlation between the shape of the shear stress-strain curve and the resulting *p-y* spring curve. Notably, both the Zhang et al. and Jeanjean et al. methodologies use the same approach to calculate both the elastic and plastic shear strains. These shear strains are then employed as inputs to compute the normalized lateral displacement (y/D) at failure, specifically for the Jeanjean et al. model [20].

In summary, Zhang et al. [38] assume a direct equivalence between shear stress and lateral bearing pressure ratios for their scaling methodology, while Jeanjean et al. [20] propose a different relationship, revealing the connection between shear stress-strain curve shape and the *p-y* spring curve. Despite the differences in their

approaches, both methodologies use similar calculations for shear strains and normalized lateral displacement at failure.

Scaling Limitations in Linear Elastic Perfectly Plastic Soil modelling

In the study conducted by Zhang et al. [38], concerns were raised regarding the suitability of scaling procedures when modelling the linear elastic perfectly plastic soil response. Despite the material exhibiting linearly elastic perfectly plastic behavior, the *p-y* response showed non-linearity due to variations in soil elements reaching the yield state at different stages. This behavior is evident in Figure 3.6, where the *p-y* model matches well with the finite element results up to a certain lateral bearing pressure mobilization level, but beyond that point, the response becomes softer, indicating a limitation of the scaling approach.

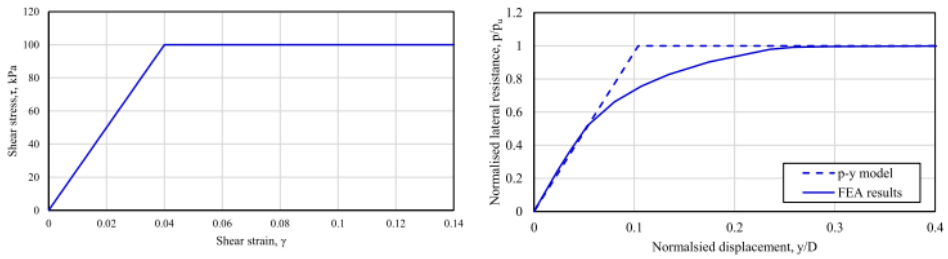

Figure 3.6: Comparison of *p-y* model prediction and finite element result for a linearly elastic perfectly plastic stress-strain response, as presented in the study of Zhang et al.[38].

To evaluate the findings and verify the observed response in Figure 3.6, the scaling methodology is employed. Since the 3D analysis models the soil as elastic perfectly plastic, the logical approach is to scale the *p-y* curve accordingly. Following the scaling procedure by Zhang et al. [38] described previously, a uniform linear elastic perfectly plastic *p-y* response is computed for all springs. Additionally, a unique y/D ratio corresponding to yielding is determined, and the elastic spring stiffness is calculated using the dimensionless stiffness coefficients provided by Wan et al. [34] for the simplified *Case 4*.

The performed static monotonic pushover analyses reveals that the calculated *p-y* response is effective for a specific range of applied loads. However, a significant deviation from the 3D results is observed for the rest of the load range. To understand

this discrepancy, the idea of defining the yielding point for every load level is conceived to detect any underlying trend. Multiple trials of the yielding point indicate a clear dependency between the applied force and the yielding force. Specifically, as the applied force increases, the yielding point (i.e., the capacity of the springs) also increases, showing a direct relationship between the two. The trend observed is depicted in Figure 3.7. This behavior, known as geometrical or structural hardening, has been documented in previous studies [12, 13]. Further details on this finding are provided in Section 3.3.2.

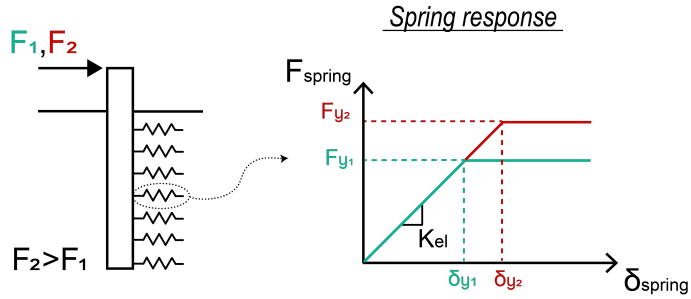

Figure 3.7: Sketch depicting the observed trend - *The higher the applied force, the higher the corresponding yielding point.*

Considering this behavior, it becomes evident that determining a single yielding point that corresponds to a good match with the 3D FE results is not achievable in the case of elastic perfectly plastic *p-y* modelling. The observed trend of increasing yielding points with higher applied forces highlights the limitations of the conventional scaling approach in capturing the non-linear *p-y* response of linearly elastic perfectly plastic soil materials.

3.3.2 Optimisation Process

The observation of load dependency in the yielding point when assuming a linear elastic perfectly plastic *p-y* response led to the idea of automating and optimizing the determination procedure for the yielding parameters in the *p-y* model. The objective is to find the optimal values for these parameters, which involves employing optimisation algorithms to explore a wide range of potential solutions through iterative analyses. These algorithms aim to identify the most favorable solution for the problem. The connection between the variables and the objective is not expressed through a specific mathematical formula but rather through a parametric model

involving numerical simulations. Consequently, the precise shape of the objective function is initially unknown.

To address such cases, black-box (or derivative-free) optimisation methods are utilized. These methods do not rely on explicit mathematical formulations and can effectively handle complex and non-linear relationships. Unlike local optimisation methods, which may get trapped in local optima, global black-box methods consider the entire design space to search for the global optimal solution. Their ability to explore the entire design space makes them well-suited for this optimisation task.

A type of global black-box optimisation method is the model-based technique. Model-based optimisation techniques involve creating surrogate models that approximate the implicit mathematical relations of simulation-based models, effectively representing the design space [15]. Surrogate models offer computational efficiency compared to time-consuming simulations, leading to faster optimisation processes. The algorithm explores various possible designs and uses them to approximate the shape of the fitness landscape. With each iteration, the surrogate model is gradually improved, enhancing the accuracy of the model during the optimisation process. This approach significantly reduces computational time, as the fitness landscape is constructed with only a few iterations, eliminating the need for repetitive and resource-intensive simulations.

Model-based optimisation methods demonstrate their capability to achieve robust results within a small number of evaluations, making them particularly advantageous for problems where simulations are time-consuming. Global model-based algorithms employ statistical techniques, like Polynomial regression, or machine-learning approaches, such as Radial Basis Functions, to construct the surrogate model. Radial Basis Functions are especially suitable for modelling complex design spaces. Despite the additional calculations required to gradually build the surrogate model, the time needed is negligible compared to the overall computational cost of simulations. Model-based algorithms can be stochastic or deterministic and show great potential for finding optimal results in various optimisation tasks.

One practical tool for model-based optimisation is RBFOpt (Radial Basis Function Optimisation), an open-source library developed for Python [23]. The Radial Basis Function model is continuously updated, identifying quickly promising areas of the design space. This tool is utilized in the current thesis to perform model-based optimisation.

Linear Elastic Perfectly Plastic (EPP) *p-y* response

The current optimization routine is designed based on modelling the linear elastic perfectly plastic (EPP) spring response. By identifying the load dependency in the yielding point, this algorithm defines the optimal spring calibration parameters for each applied load under examination. As discussed in Section 3.3.1, the elastic spring stiffness (K_{el}) is obtained from the study by Wan et al. [34], and therefore, this value is already known. The unknown quantity is the yielding deformation (δ_y) (or yielding force, F_y) of the *p-y* response, as illustrated in Figure 3.8.

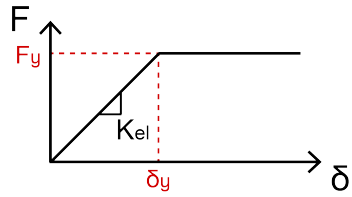

Figure 3.8: Sketch depicting the uniaxial *EPP p-y* spring modelling.

In essence, the core logic of this optimization routine is as follows. For each load level, the algorithm calculates the yielding point (δ_y or F_y), that minimizes the discrepancy between the results obtained from the 1D and 3D analyses.

The yielding deformation (δ_y) serves as the sole variable, precisely determined by the algorithm to achieve the best match between the 3D and 1D responses. Thus, the optimization's objective is to minimize the mismatch in the responses. This objective function, or error, is formulated based on Versteijlen et al.'s approach [32] and is expressed by Equation 3.7. The quantification of the match involves computing the absolute deviation in the deflection (u) and rotation (u'') profiles with respect to the corresponding values obtained from the 3D FE analyses along the entire length of the monopile. For the present calculation, the fit of deflection and rotation is given equal weight. The error formulation utilized in this study is known as the relative Mean Bias Error (rMBE), a statistical metric that measures the deviation of the model's predictions from the observed values. Notably, in his later doctoral dissertation [31], Versteijlen introduced an extended error formulation that incorporates two additional parameters: the slope of the deflection curve and the curvature. Equal weighting was applied to all four components to attain a more comprehensive error assessment. However, in this master's thesis, the methodology follows Versteijlen's earlier research trajectory [32]. This approach proves advantageous in terms

of computational efficiency, ensuring a faster optimization routine.

$$Error_{u+u''} = Error_u + Error_{u''} = \frac{\sum_{i=0}^{i=L} |u_{3D,i} - u_{1D,i}|}{2 * \sum_{i=0}^{i=L} |u_{3D,i}|} + \frac{\sum_{i=0}^{i=L} |u''_{3D,i} - u''_{1D,i}|}{2 * \sum_{i=0}^{i=L} |u''_{3D,i}|} \tag{3.7}$$

By utilizing this error formulation, the optimization algorithm strives to find the yielding deformation values that provide the best agreement between the 3D and 1D results for both deflection and rotation profiles. It is important to acknowledge that different researchers may prioritize various aspects of soil-monopile interaction and accordingly define their objective functions. For instance, Wan et al. [34] defines the objective function as the summation of the relative error between the lateral and rotational monopile head stiffness, thereby quantifying the match at a single point, namely the monopile head. Conversely, Rahmani et al. [25] takes into account the monopile head displacement and the maximum bending moment developed along the monopile shaft, not explicitly relying on a local check. In this master's thesis, the objective function quantifies the best match along the entire monopile shaft, and then, through post-processing of the results, the local monopile head response is assessed. This approach allows for a comprehensive evaluation of the soil-monopile interaction along the entire length of the structure, leading to a more detailed understanding of its behavior under various loading conditions.

Having clarified the algorithm logic, ten optimization routines were executed, encompassing five monopile geometries and two lateral load eccentricities for each geometry, as stated in Section 3.1. The maximum static monotonic load investigated corresponds to the load level that induces either a 2° rotation at the monopile head or a deflection equal to 10% of the monopile's diameter at the monopile head, whichever occurs first. These values are commonly used in practice as criteria for the ultimate limit state (ULS). For all cases examined, the condition of 2° rotation at the monopile head was reached first, thereby establishing the F_{max} value. In all susequent plots, the applied force $F_{applied}$ is normalised with respect to the maximum force F_{max} and denoted as ζ_b. Furthermore, an upper limit of 50% is set for the acceptable error. Figure 3.9 presents the results obtained from the optimization routines for all monopiles and eccentricities.

The decision to present the optimization results in two separate plots is deliberate, as the error distribution over the normalised applied load range response exhibits substantial differences among the examined monopile geometries. Notably, the shape of the curve varies significantly between the monopile geometries with L/D

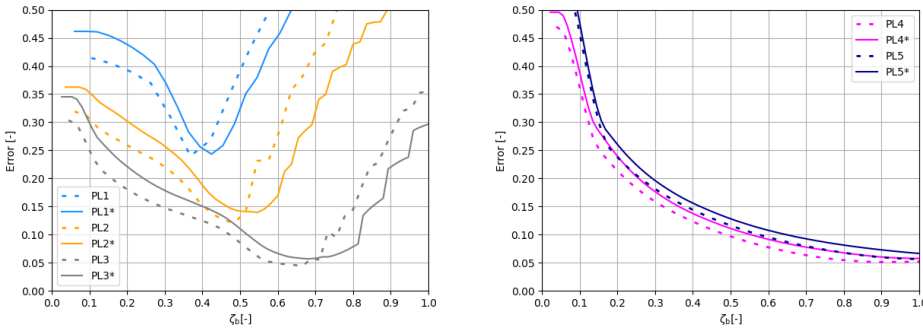

(a) Monopiles with L/D ratios of 2, 3, and 4.

(b) Monopiles with L/D ratios of 6 and 8.

Figure 3.9: Error evolution for monopile geometries with (a) low L/D ratio and (b) high L/D ratio across the entire range of applied loads, using *EPP p-y* spring response.

ratios lower than 4 and those with L/D ratios higher than 6. The outcomes consistently reveal that the 'more flexible' piles exhibit a lower overall error across the load range. This trend can be attributed to the potential adequacy of lateral *p-y* springs in representing the response. Stated differently, the moment developed along the monopile shaft and the pile toe kick often observed in rigid monopiles are less pronounced for higher L/D ratio monopiles [4]. The behavior of monopile geometries with lower L/D ratios resembles that of caisson foundations, as mentioned in [17]. An alternative explanation for this pattern may be attributed to the differing failure mechanisms. In shallower depths, where soil surface influences the failure mechanism, failure tends to adopt a wedge-like pattern. Conversely, in deeper depths, the flow around failure mechanism prevails [26].

Considering PL4's relative pile stiffness of $K_r = 0.0022$ as mentioned in Table 3.1, it is positioned just below the semi-rigid threshold. This means it leans more towards flexible behavior. PL5, the longer pile, falls in the same category. Also, it is worth noting that the *PISA design model* [7] was designed for piles with L/D ratios from 2 to 6. In contrast, the study by [34] examined L/D ratios from 2 to 8. This difference shows that L/D ratios alone cannot determine if a pile's behavior is rigid, intermediate, or flexible. In fact, soil characteristics play a role in the pile's response, as shown in Equation 2.1, where soil stiffness E_{soil} is included in the formulation. Thus, given the current problem characteristics, L/D ratios exceeding 6 might extend

beyond the established boundaries of the semi-rigid zone.

Furthermore, it is noteworthy that despite the increase in pile length from PL4 to PL5, both monopiles exhibit a 2° rotation at the monopile head under the same lateral load, as illustrated in Figure 3.10. This observation suggests that the increase in pile length may not have had a significant impact on the deflection and rotation at the monopile head. In other words, it raises the possibility that the critical (or active) pile length, as discussed in [4, 3], might have already been exceeded for an L/D ratio of 6.

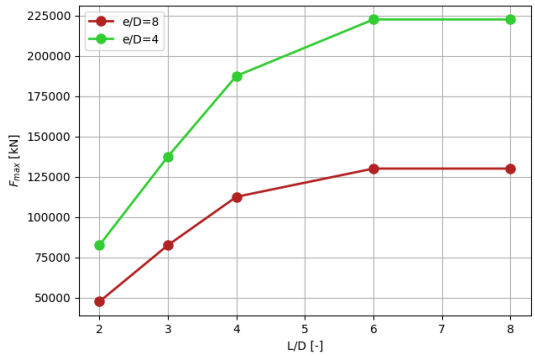

Figure 3.10: F_{max}, representing the ULS load, calculated for all scenarios under examination.

After the examination of the dissimilarity in the error evolution shape, as depicted in Figure 3.9, a specific value of ζ_b=0.5 was chosen to calculate the yielding force per monopile length. The results are presented in Figure 3.11. Notably, for aspect ratios greater than 3, the normalised yielding force remains consistent regardless of the examined load eccentricity. The normalization of the yielding force, essentially signifying a distributed lateral load, follows the guidelines detailed in [8]. It is important to restate that the assumption of a uniform soil layer and thus the modelling of a pressure-independent material aligns more closely with the behavioral characteristics of clayey soil. This interpretation leads to the modelling of the soil as having properties reminiscent of clayey material, thereby justifying the utilization of the capacity of the soil, represented as τ_{max}, in the graph for accurate depiction.

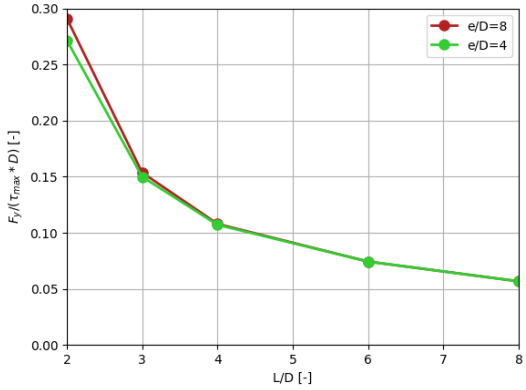

Figure 3.11: Yielding force per monopile length for *EPP p-y* spring modelling and for $\zeta_b = 0.5$.

Bilinear (BL) *p-y* response

The EPP modelling of springs presents a significant drawback, as it relies on load-dependent spring calibration to achieve reliable results. This practicality issue arises because precise knowledge of the applied load at the soil-monopile structure is essential for calibrating the springs to match the desired response accurately. To overcome this limitation and ensure a more versatile approach, it becomes crucial to define and calibrate a spring material capable of encompassing the entire load range without being affected by load variations. Consequently, the load dependency on spring parameters must be eliminated. In light of this consideration and after observing the phenomenon of 'pseudo' hardening, as discussed in Section 3.3.2, the concept of modelling a bilinear *p-y* response emerged as an innovative solution.

It is important to note that this 'pseudo' hardening behavior is not an actual soil hardening property, but rather a consequence of the actual tri-dimensionality of the stress state and the presence of 'structural redundancy' in the system. This phenomenon leads to an apparent hardening in the shear behavior, as explained in the work of Di Prisco et al. [12]. In the elastoplastic regime, stress redistribution allows stresses to go beyond the first yielding point, which explains the observed 'pseudo' hardening behavior, as stated in the work of Di Prisco & Pisanò [13].

To develop the bilinear (BL) spring response, an alternative approach is adopted by combining two separate material objects in parallel. The first spring utilizes an elastic uniaxial material (E), while the second incorporates an elastic perfectly plastic uniaxial material (EPP), as illustrated in Figure 3.12. This configuration allows for the representation of both linear elastic and linear hardening spring behavior. In this context, the stiffness of the elastic branch is already known (K_{el}), following the methodology adopted in the study by Wan et al. [34]. However, the stiffness of the hardening branch (K_h) and the point of first yielding (δ_y) become the two variables in this optimization problem. The primary objective remains consistent and is expressed by Equation 3.7, which captures the minimization of the error between the 1D model predictions and 3D results.

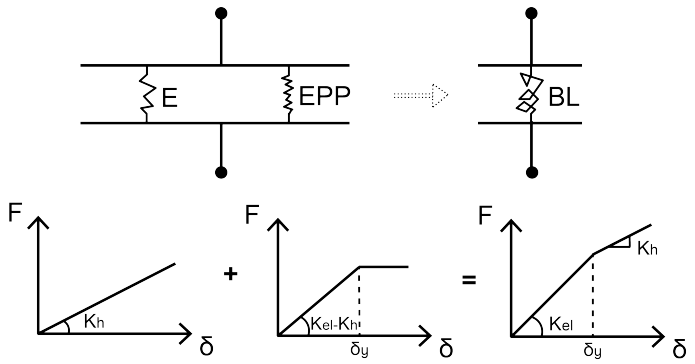

Figure 3.12: Sketch depicting the BL *p-y* spring modelling.

The optimization routine is subsequently revised with the following core logic. Bounded by the load range, from zero to the ultimate limit state load, the algorithm calculates a single set of variables, namely the point of initial yielding (δ_y) and the inclination of the hardening branch (K_h), that minimize the discrepancy between the results obtained from the 1D and 3D results. Figure 3.13 presents the results obtained from the optimization routine for all monopiles and eccentricities.

The discrepancy in the error evolution between the 'low' and 'high' aspect ratios becomes also evident in the current *p-y* spring calibration. Notably, the overall error across the entire load range is either very close or even lower than the one obtained from the EPP *p-y* modelling. This promising outcome suggests that a single set of parameters can be calibrated for the material model, offering commendable accuracy across the range of loads.

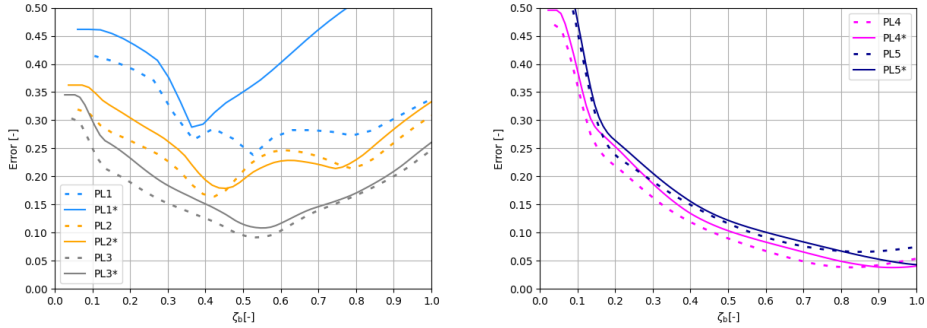

(a) Monopiles with L/D ratios of 2, 3, and 4.

(b) Monopiles with L/D ratios of 6 and 8.

Figure 3.13: Error evolution for monopile geometries with (a) low L/D ratio and (b) high L/D ratio across the entire range of applied loads, using BL *p-y* spring response.

For a preliminary insight, Figure 3.14 displays the match of PL4 at the monopile head, along with the deflection and rotation profiles for ζ_b=0.5. As presented, both the global response of the monopile head and the displacement profiles exhibit excellent agreement with the 3D results. This encouraging outcome signifies the successful selection of BL model parameters.To further assess the performance of all examined 1D spring models, the match on the monopile head concerning deflection and rotation will be thoroughly evaluated in Section 3.3.3.

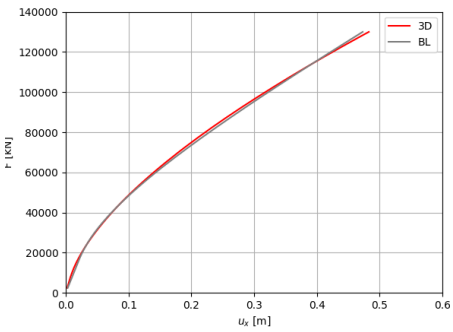

(a) Displacement at mudline.

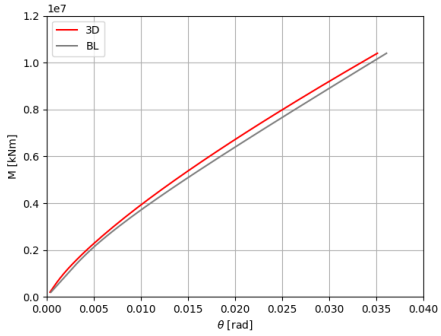

(b) Rotation at mudline.

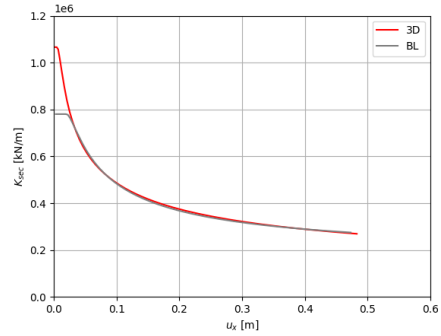

(c) Displacement-based secant stiffness.

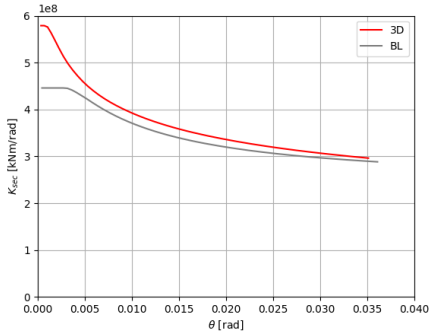

(d) Rotation-based secant stiffness.

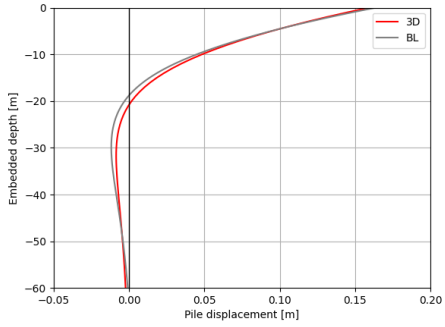

(e) Displacement profile.

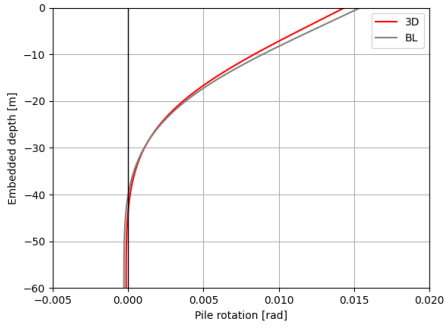

(f) Rotation profile.

Figure 3.14: BL material model application for PL4: (a)-(d) Global response of the monopile at mudline & (e)-(f) Deflection and rotation profiles for ζ_b=0.5.

It is of significant engineering interest to assess the ratio between the two branches of the bilinear response. Specifically, the ratio of the hardening to the elastic stiffness is calculated and illustrated in Figure 3.15. Upon examination, it is observed that monopile geometries with L/D ratios lower than 3 exhibit an ambiguous response, likely attributed to the limitation of *p-y* lateral springs alone in capturing their behavior, as discussed in the previous section. However, for monopiles with L/D ratios greater than 3, an apparent pattern emerges.

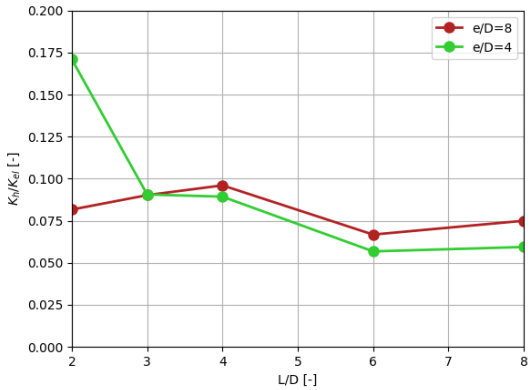

Figure 3.15: Ratio of the hardening to elastic spring stiffness for BL p-y spring modelling.

In addition to assessing the K_h variable, it is crucial to evaluate the yielding point, which serves as the second variable in the bilinear modelling. By utilizing the known values of K_{el} and the point of initial yielding δ_y, the yielding force F_y can be computed by multiplying these values and then dividing by the monopile's length. The normalized yielding force across the examined aspect ratios is depicted in Figure 3.16. As depicted, a high degree of agreement is observed for all examined e/D values, particularly for L/D ratios equal to or greater than 3.

The procedure for modelling the bilinear *p-y* response can be outlined as follows for a given L/D and e/D:

1. Compute the K_{el} [kN/m] value by adopting the dimensionless K_{py}^{S} value from Figure 2.2 ([34]).
2. Utilize Figure 3.15 and the known K_{el} [kN/m] to determine the K_h [kN/m].

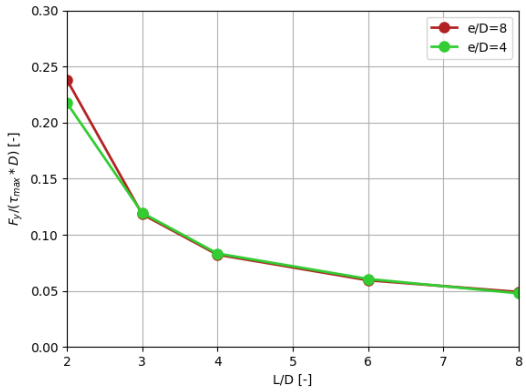

Figure 3.16: Normalised yielding force per monopile length for BL p-y spring modelling.

3. Refer to Figure 3.16 to define the F_y [kN/m].

This sequential process provides a structured approach to determine the necessary parameters for bilinear *p-y* modelling. It is important to note that this methodology is applicable when $3 \leq \frac{L}{D} \leq 8$, and when $4 \leq \frac{e}{D} \leq 8$.

Exponential (SL) *p-y* response

A more advanced approach is considered next, aiming to enhance the plastic response of the springs. While the bilinear model employed earlier provides a reasonable approximation, the utilization of an exponential model is anticipated to yield closer alignment with the actual soil behavior. Consequently, the Suryasentana and Lehane's (SL) *p-y* model, originally developed for laterally loaded piles in sand under static loading conditions, will be employed [29]. Given the primary focus of this thesis on the analysis of lateral loaded piles under static monotonic loading, the SL model is deemed a suitable choice. Additionally, the potential application of this model reformulation by Kementzetzidis et al. [21], for investigating soil-monopile interaction under cyclic and seismic loading conditions in the future, is of particular interest. However, for the present master's thesis, which is restricted to static loading scenarios, the original SL model will be utilized. This model is characterized by the following *p-y* relationship:

$$y = D\left[-\frac{1}{a}\ln\left(\frac{p_u - p}{p_u}\right)\right]^{\frac{1}{m}} \tag{3.8}$$

In Equation 3.8, D represents the diameter of the monopile, while α and m are dimensionless parameters. The α parameter relates to the plastic stiffness, while the m parameter affects the curvature of the *p-y* curve. The ultimate soil reaction force per unit length is denoted as p_u. The diameter of the pile is a known constant and is consistent at 10m across all examined monopile geometries. The variables of interest in this model and optimization problem are p_u, α, and m. Since the SL model incorporates plasticity effects, an elastic spring will be introduced to accurately simulate the response. Specifically, an elastic uniaxial material will be combined in series with the SL uniaxial material, forming the composite material employed by the spring. This configuration is depicted in Figure 3.17.

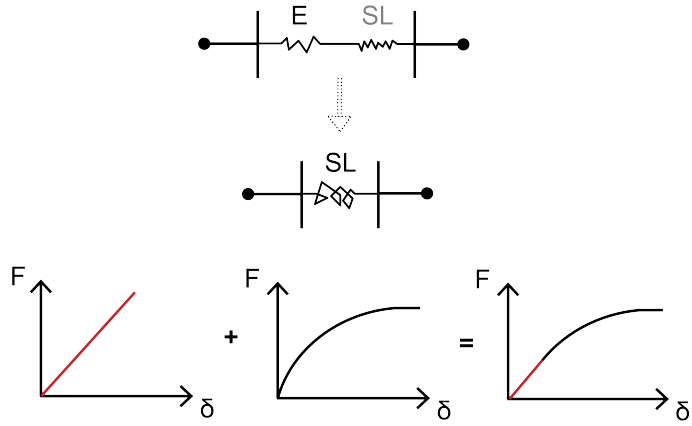

Figure 3.17: Sketch depicting the SL *p-y* spring modelling.

The calibration of the elastic material (K_{el}) is derived using the approach outlined in the study by Wan et al. [34]. As previously noted, the parameters p_u, α and m that define the SL material properties are unknown, making them the three variables of interest in this optimization endeavor. The fundamental goal remains unchanged, and it is expressed by Equation 3.7, which represents the aim of reducing the difference between predictions from the 1D model and the real 3D results.

Similar to the optimization approach for the BL model, the SL optimization routine adopts the following logic. Bounded by the load range, from zero to the ultimate limit state load, the algorithm calculates a single set of variables, namely the p_u, α and m, that minimize the discrepancy between the results obtained from the 1D and 3D results. The outcomes of the optimization routine for all monopiles and eccentricities are depicted in Figure 3.18.

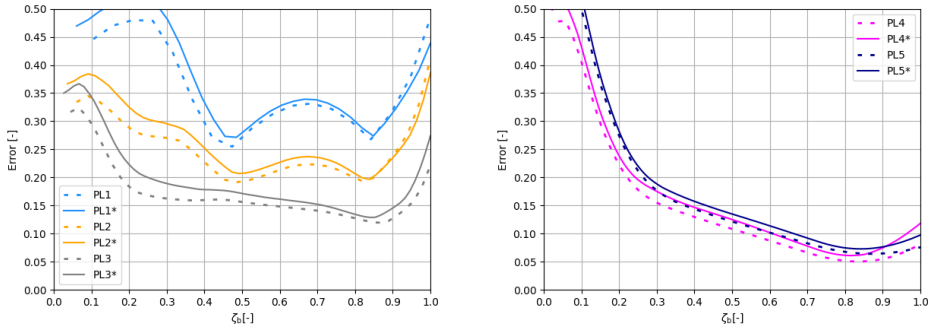

(a) Monopiles with L/D ratios of 2, 3, and 4.

(b) Monopiles with L/D ratios of 6 and 8.

Figure 3.18: Error evolution for monopile geometries with (a) low L/D ratio and (b) high L/D ratio across the entire range of applied loads, using SL *p-y* spring response.

The error distribution is once again categorized into 'low' and 'high' aspect ratios. However, these distributions reveal a noticeable trend in the evolution of errors across all examined monopiles. Specifically, as the L/D ratio increases, the curve gradually levels off and shifts towards lower error values, for higher ζ_b.

When evaluating the overall error magnitude across the entire load spectrum, the average error for the SL model (Figure 3.18) is slightly higher than that of the BL model (Figure 3.13). This finding is intriguing because, even though the SL model offers more flexibility with its three parameters, it doesn't seem to produce significantly different error results when compared to the BL model, which uses only two parameters.

There are two possible reasons for this observation. First, it may be attributed to computational limitations of the optimization algorithm, which struggles to accurately identify the three variables of the SL model, especially given that two of these

variables (particularly α with two decimal places and m with four decimal places) are highly sensitive to slight modifications. This makes the optimization process computationally expensive and the identification of the optimal solution challenging.The second reason is more conceptual. It's found that a specific set of parameters can optimally describe a particular portion of the response. However, in this thesis, the objective is to define a single set of parameters that works optimally across the entire load range, from zero to ULS load. Consequently, the error resulting from the SL optimization cannot be very small since it represents an average best solution that accounts for the entire load range.

Having provided these possible explanations, it's clear that the evolution of errors alone doesn't offer a definitive insight into the achieved match. As an illustrative example, the alignment achieved for PL4 is depicted in Figure 3.19.

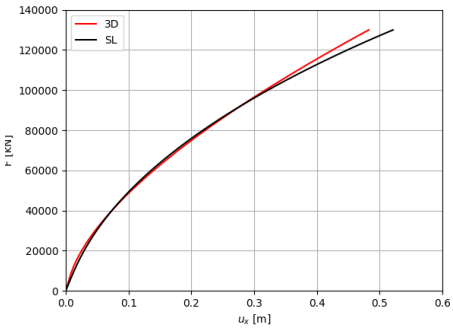

(a) Displacement at mudline.

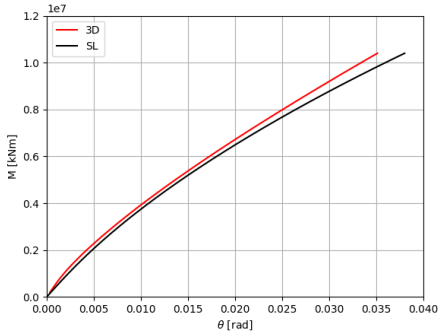

(b) Rotation at mudline.

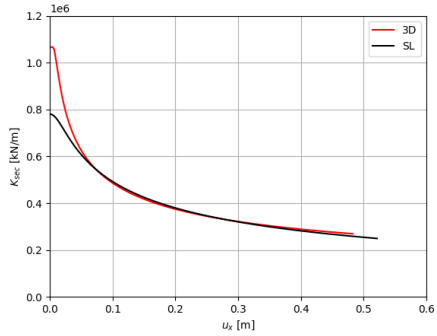

(c) Displacement-based secant stiffness.

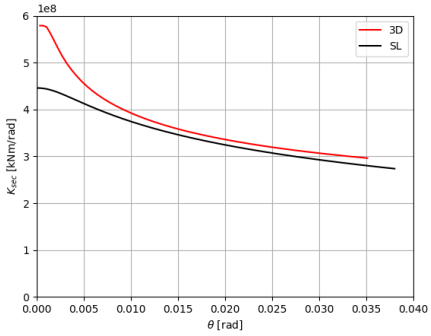

(d) Rotation-based secant stiffness.

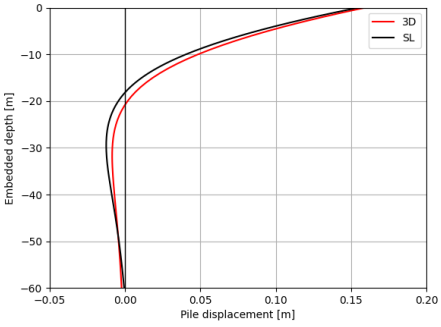

(e) Displacement profile.

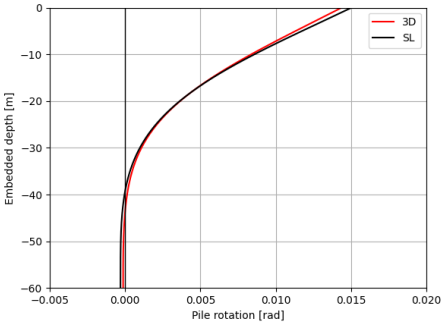

(f) Rotation profile.

Figure 3.19: SL material model application for PL4: (a)-(d) Global response of the monopile at mudline & (e)-(f) Deflection and rotation profiles for ζ_b=0.5.

As shown in Figure 3.19, the match is very good, affirming a successful calibration of the employed springs. As previously mentioned, the subsequent section will delve into the assessment of monopile head response to explore the local alignment at that critical point for all monopiles examined. Encouragingly, the algorithm has consistently identified a set of variables that yields reliable outcomes for the analyzed cases.

At this point, it becomes intriguing to evaluate the output variable values derived from the optimization algorithm. Firstly, the normalized ultimate soil reaction force (p_u) is depicted in Figure 3.20. As observed, the decreasing trend of p_u with increasing L/D ratio is evident in this plot as well. Notably, the obtained graph closely resembles the yielding force graph of the BL modelling, as depicted in Figure 3.16. It's worth highlighting that the alignment is consistent for L/D values exceeding 3, regardless of the examined eccentricity.

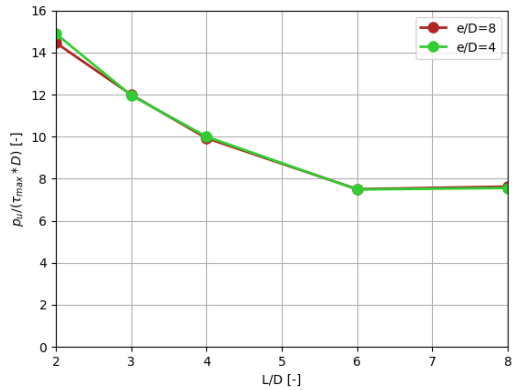

Figure 3.20: Normalised ultimate soil reaction force per unit length for SL *p-y* spring modelling.

The obtained α and m values from the optimization routine are showcased in Figure 3.21. Notably, both graphs exhibit a consistent trend, ultimately converging to a singular value for L/D ratios exceeding 6. Furthermore, the parameter ranges for α and m are established. Specificaly, the α parameter spans from 4 to 6, while the m parameter ranges between 0.34 and 0.36, encompassing all the considered aspect ratios and load eccentricities. The values of α and m can be directly interpreted from

the graphs in Figure 3.21.

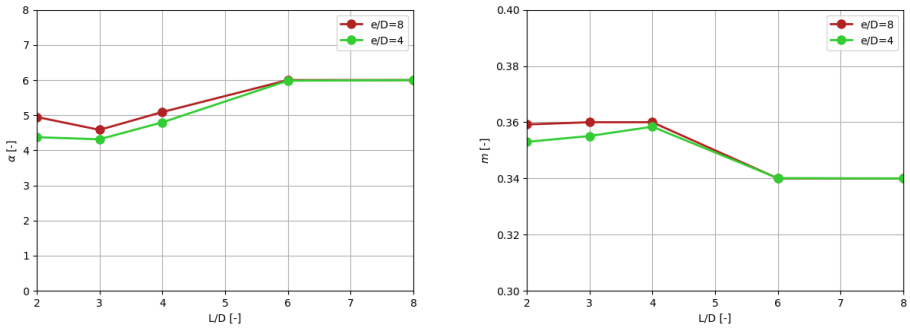

(a) α parameter **(b)** m parameter

Figure 3.21: Dimensionless parameters (a) α and (b) m, as derived from the optimisation routine of the SL p-y spring modelling.

The process of modelling the SL *p-y* response can be summarized as follows, considering a given L/D and e/D:

1. Compute the K_{el} [kN/m] value by adopting the dimensionless K_{py}^{S} value from Figure 2.2 ([34]).

2. Refer to Figure 3.20 to define the ultimate soil reaction force p_u [kN/m].

3. Define the dimensionless parameters α and m from Figures 3.21a and 3.21b, respectively.

This step-by-step method presents a structured strategy to ascertain the required parameters for exponential SL *p-y* modelling.

3.3.3 Comparison of the 1D Spring Models

Initially, the error distributions of all considered material models will be visually presented together in a single graph, focusing on a specific pile for the purpose of comparison. In this context, PL3 monopile has been selected. The error evolution profiles for the EPP, BL, and SL models are displayed in Figure 3.22.

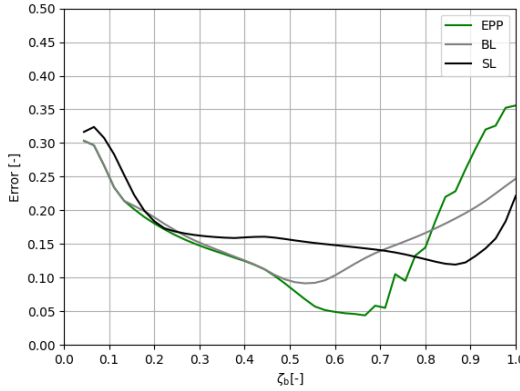

Figure 3.22: Error comparison on PL3 monopile: EPP, BL, and SL material models.

As depicted in Figure 3.22, both the EPP and BL models exhibit identical errors during the initial loading phase, corresponding to low ζ_b values. This uniformity suggests a linear soil response and absence of plasticity at this stage. However, the discrepancy in the SL error distribution during this initial phase can be attributed to the calibration approach employed. The investigation revealed that certain parameter combinations within the SL model can precisely align with the early error distribution, similar to the other two curves. Yet, this parameter set resulted in significantly higher errors for higher ζ_b values, deviating from the rest of the predictions. This observation underscores the common engineering practice of calibrating material models to perform well within specific displacement ranges. In this case, the chosen SL parameter values were deliberately selected to ensure consistent performance across the entire load range, aligning with the objective of this master's thesis.

It is important to highlight that relying solely on the error value does not offer a complete understanding of the achieved alignment. Consequently, for a more thorough evaluation of the model's precision, the global response at the mudline level will be computed and compared. This assessment will encompass factors such as deflection, rotation, and their corresponding secant stiffnesses, ultimately comparing these findings with the 3D results for a comprehensive analysis.

This section of the thesis showcases the outcomes concerning monopiles labeled

as PL1, PL3 and PL5. The respective outcomes are visually depicted in Figures 3.24, 3.25 and 3.26, which can be found on the last pages of this section. These selections were made with the intention of providing a representative and gradual sample, enabling the detection of response differences while avoiding excessive intricacies. The load application point was demonstrated not to impact the observed trends. This implies that monopiles with the same L/D ratio but different e/D exhibit qualitatively similar responses at the monopile head. To illustrate this, the results for PL1*, PL3*, and PL5* are provided in the Appendix A.

Upon examination of the alignment to the 3D results, ranging from the stubbier monopile, PL1, to the more flexible monopile, PL5, a notable trend becomes apparent. The best alignment, encompassing both deflection and rotation at the monopile head, is achieved by the more flexible pile. This observation can be attributed to the fact that relying solely on lateral *p-y* springs yields more precise results for monopiles with higher L/D ratios, where the effects at the base and the developed shaft moment are less pronounced. In simpler terms, the utilization of exclusively lateral *p-y* springs does not lead to significantly inaccurate predictions of the response for the higher L/D piles.

Nonetheless, the secant stiffness based on initial displacement is most accurately represented by the monopile with the lower L/D ratio. This phenomenon can be explained by considering the calibration of elastic stiffness, as guided by Wan et al. [34], whose analyses were based on an ideally rigid pile. Consequently, it is logical to expect a better representation of the response of monopiles with lower L/D ratios within the realm of small displacements, given their comparatively more 'rigid' behavior.

Conversely, the capture of rotation-based secant stiffness, particularly for minor rotations, faces challenges even in the context of the most 'rigid' pile. This challenge arises from the reliance solely on lateral shaft springs in the present study. It is anticipated that incorporating rotational shaft springs into the 1D modelling will likely yield a more accurate match. An overview of the obtained response for three monopile geometries examined in terms of normalised moment and rotation is presented in Figure 3.23. It is important to note that the critical criterion defining the ULS condition is a maximum rotation (θ_{ult}) of 2° at the monopile head. This value is used to normalize the obtained rotation values for comparison. As previously highlighted, it becomes evident from this graph that as the L/D ratio decreases, the curve steepens. Consequently, it is clear that the 1D models face challenges in accurately capturing the intricate 3D response of the lower L/D monopiles.

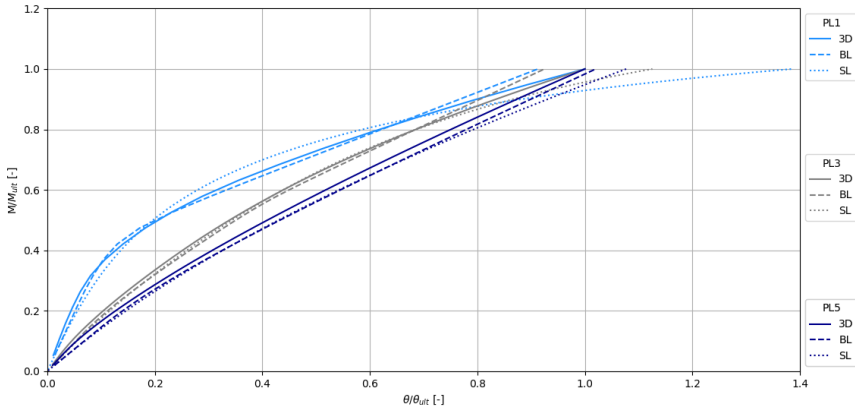

Figure 3.23: Normalised moment against normalised rotation for PL1 (L/D=2), PL3 (L/D=4) and PL5 (L/D=8).

Subsequently, a comparison between the BL and SL 1D *p-y* models is conducted to discern their respective performance and determine which model fares better, given the ambiguity stemming from the error distribution. Notably, both models exhibit a remarkably strong agreement with the reported 3D response.

Upon comparing the outcomes of the BL and SL modelling with the 3D results, a consistent pattern emerges. The BL model consistently yields deflection values smaller than those predicted by the 3D simulations, which runs counter to safety considerations. Conversely, the SL model tends to overestimate both the final deflection and rotation at mudline, thus adopting a conservative approach that aligns favorably with safety protocols. Consequently, the SL model exhibits a distinct advantage in this context.

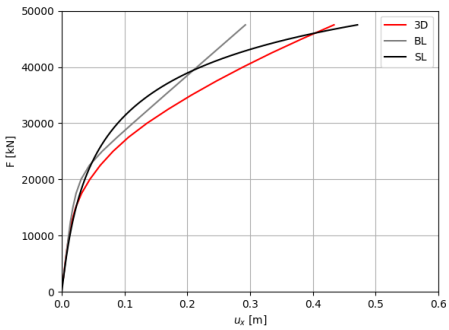

(a) Displacement at mudline.

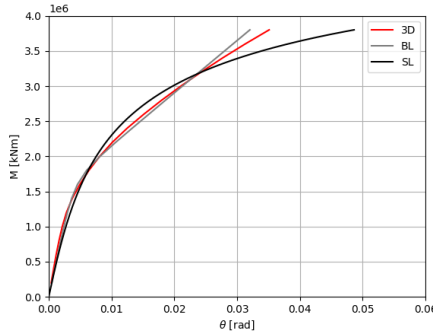

(b) Rotation at mudline.

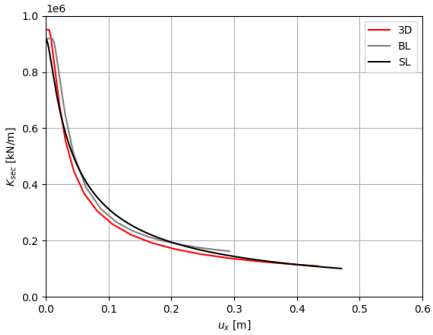

(c) Displacement-based secant stiffness.

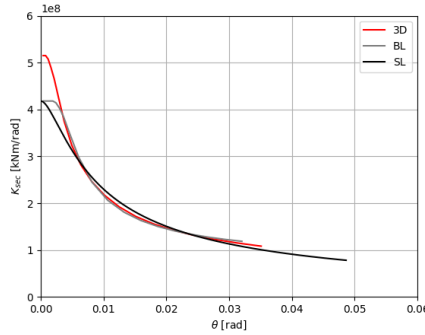

(d) Rotation-based secant stiffness.

Figure 3.24: Global response of monopile PL1 at mudline.

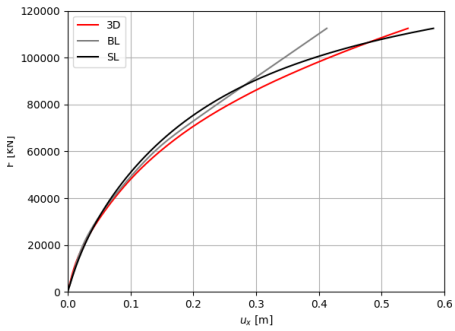

(a) Displacement at mudline.

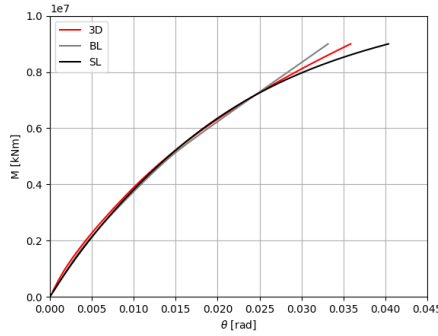

(b) Rotation at mudline.

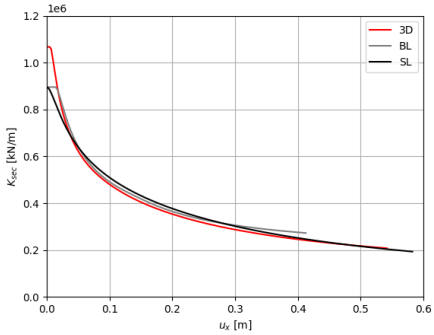

(c) Displacement-based secant stiffness.

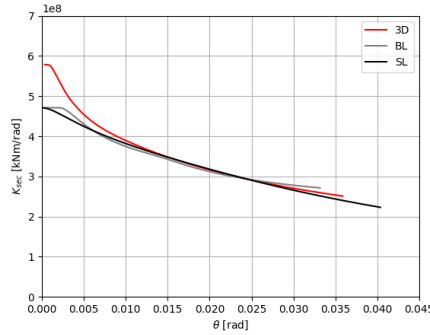

(d) Rotation-based secant stiffness.

Figure 3.25: Global response of monopile PL3 at mudline.

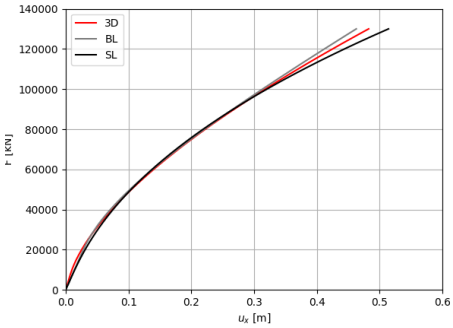

(a) Displacement at mudline.

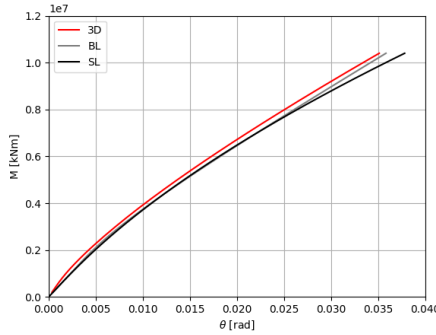

(b) Rotation at mudline.

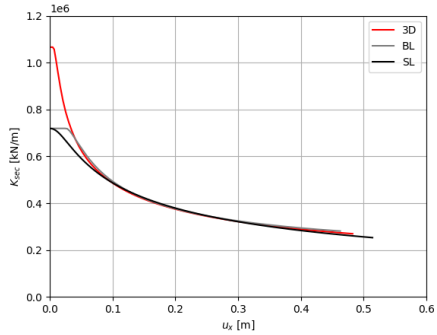

(c) Displacement-based secant stiffness.

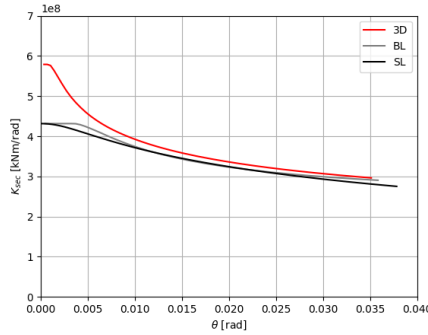

(d) Rotation-based secant stiffness.

Figure 3.26: Global response of monopile PL5 at mudline.

3.4 Case Study

To validate the applicability of the 1D modelling methodologies proposed in the preceding sections, a new analysis is conducted with altered parameters. While the superstructure characteristics remain unchanged, as detailed in Table 2.2, modifications are introduced to both pile and soil characteristics. These updated attributes are outlined in Tables 3.2 and 3.3. The newly considered pile, designated as CS, is subjected to lateral loading with an eccentricity of 48m, following the utilization of D=8m in the calculation, where e/D=6. The choice of e/D aligns with the range of eccentricities previously studied (4 and 8), rendering the proposed methodology suitable for application. Notably, CS possesses a distinct L/D ratio of 5, a value not previously explored.

Table 3.2: Case Study - CS characteristics

Notation	Diameter D [m]	Length L [m]	L/D [-]	e/D [-]	Wall thickness t [mm]	E_{pile} [GPa]	I_{pile} [m^4]
CS	8	40	5	6	80	210	15.61

Table 3.3: Case Study - Soil properties

Bulk Density [Mg/m^3]	Poisson's Ratio ν [-]	G_{soil} [MPa]	Strength τ_{max} [kPa]
1.61	0.30	93	87.5

3.4.1 Application of EPP methodology for 1D soil modelling

As outlined in the preceding sections, the initial approach to modelling elastoplastic response in the 1D framework involves the EPP *p-y* response. Following the steps detailed in Section 3.3.2, the EPP modelling essentially involves determining the yielding point for each load level, ranging from zero up to F_{max}. It is worth noting that the maximum lateral load applied is determined by the load level at which a 2° rotation is observed at the monopile head, as per the findings from the 3D analysis. The EPP optimization was executed and the yielding deformations were computed for each load level. To validate the utility of the normalised graph presented earlier, the optimised yielding force corresponding to ζ_b=0.5 was calculated and incorporated in Figure 3.11, which is now depicted in Figure 3.27. Notably, the optimised

data point, corresponding to CS and ζ_b=0.5, closely aligns with the prediction. This encouraging observation indicates the consistency of the conducted analyses, suggesting their applicability across different scenarios. To enhance accuracy and gain a more comprehensive understanding of the curve's behavior, further analyses with diverse property variations are recommended.

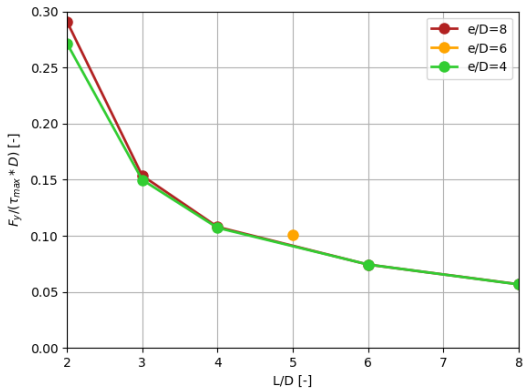

Figure 3.27: Yielding force per monopile length for *EPP p-y* spring modelling and for $\zeta_b = 0.5$, including data for CS.

To illustrate the discrepancy between the prediction and the optimized calibration, the latter of which is indicated by the orange bullet point in Figure 3.27, the deflection and rotation distributions with depth have been computed and are showcased in Figure 3.28. Evidently, the predicted response falls short of aligning with the 3D profiles as effectively as the optimized response does, both in terms of deflection and rotation distribution. Nonetheless, the degree of misalignment is not overly significant, rendering it a reasonably reliable representation. Qualitatively, the error associated with the predicted response is approximately 13%, whereas the error linked to the optimized response is around 8%. It is important to highlight that due to the EPP model having only one variable for calibration, it presents a greater challenge and is anticipated to achieve a less successful alignment with the response, particularly when compared to more advanced BL and SL models.

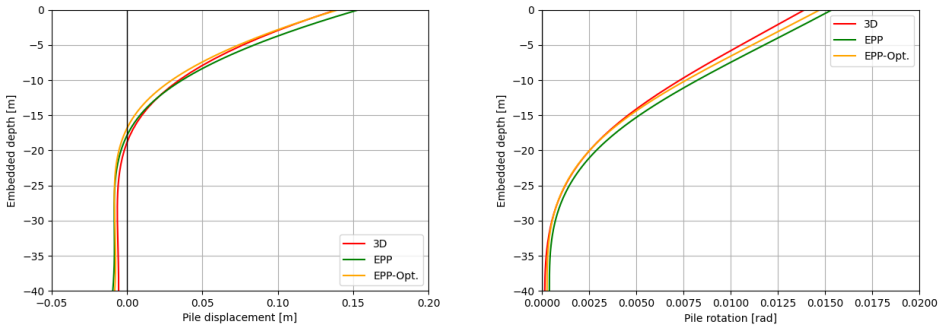

(a) Displacement profile.

(b) Rotation profile.

Figure 3.28: Deflection and rotation profiles along the length of CS, for ζ_b=0.5: EPP material model calibrated based on Figure 3.27 (green line) and calibrated upon optimisation (orange line).

3.4.2 Application of BL methodology for 1D soil modelling

Moving on to the BL *p-y* response, as detailed in Section 3.3.2, the procedure outlined at the end of that section will be followed. Consequently, in line with the steps previously elucidated:

For L/D=5 & e/D=6:

1. From Figure 2.2, $K_{py}^{S} = 7.61 \Rightarrow K_{el} = K_{py}^{S} \times G_{soil} \times dz = 176482$ kN/m.
2. From Figure 3.15, $K_h = 0.075 \times K_{el} = 13236$ kN/m.
3. From Figure 3.16, $F_y = 0.072 \times \tau_{max} \times D = 50.4$ kN/m.

Following the step-by-step methodology, the two parameters of the BL model, namely K_h and δ_y, are computed and employed in the model's calibration. The error distribution, resulting from the analysis utilizing these parameters, aligns closely with the established pattern observed in the EPP modelling's error distribution, as depicted in Figure 3.29. This encouraging observation signifies that the selected parameters for the BL model likely lead to satisfactory results.

Notably, the predicted deflection and rotation at the monopile head, and the respective secant stiffnesses, exhibit a remarkable level of accuracy, as illustrated in

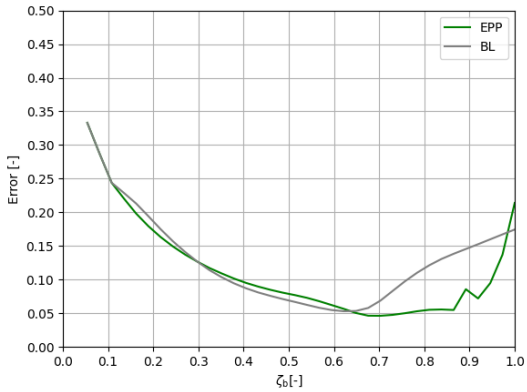

Figure 3.29: Error comparison on CS monopile: EPP and BL material models.

Figures 3.30a, 3.30b, 3.30c and 3.30d. To assess the extent of improvement achieved through optimization, the optimization algorithm is executed, resulting in an error difference of less than 0.5% between the optimized response and the prediction. Given the exceptional level of agreement, it is unnecessary to provide an exclusive report of the optimized variables.

Furthermore, the alignment of the deflection and rotation distributions with the 3D counterparts for a specific load level are showcased. Particularly, the profiles along the length corresponding to $\zeta_b = 0.5$ are depicted in Figures 3.30e and 3.30f. As demonstrated, the correspondence is exceptionally strong throughout the pile's length.

Consequently, the suggested step-by-step empirical design process, coupled with the graphical representations, underscores the satisfactory performance of the BL model across various soil properties, monopile geometries, and lateral load eccentricities.

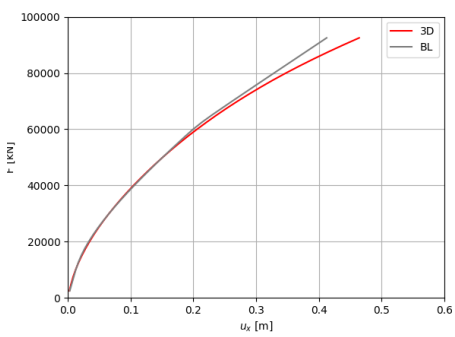

(a) Displacement at mudline.

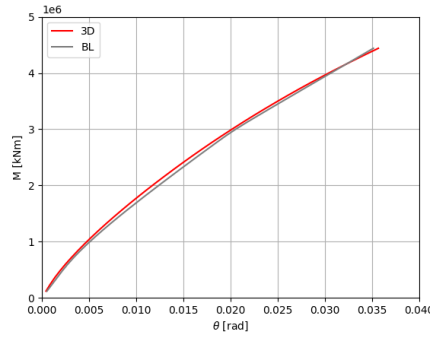

(b) Rotation at mudline.

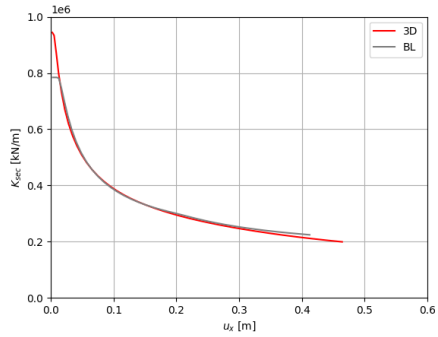

(c) Displacement-based secant stiffness.

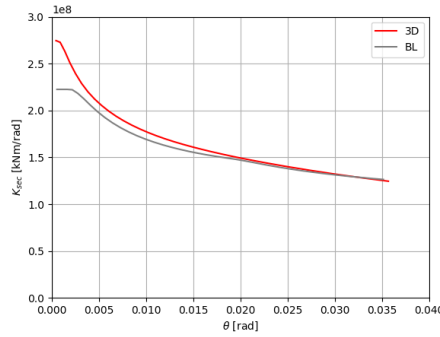

(d) Rotation-based secant stiffness.

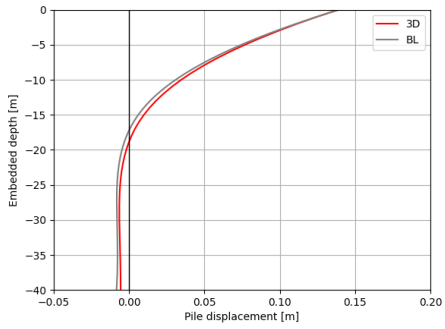

(e) Displacement profile.

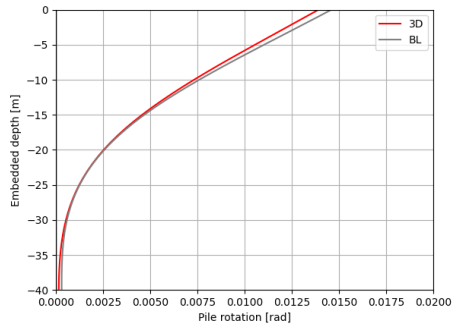

(f) Rotation profile.

Figure 3.30: BL material model application for CS: (a)-(d) Global response of the monopile at mudline & (e)-(f) Deflection and rotation profiles for ζ_b=0.5.

3.4.3 Application of SL methodology for 1D soil modelling

Next, the methodology outlined in Section 3.3.2, for modelling the SL *p-y* response will be followed:

For L/D=5 & e/D=6:

1. From Figure 2.2, $K_{py}^{S} = 7.61 \Rightarrow K_{el} = K_{py}^{S} \times G_{soil} \times dz = 176482$ kN/m.
2. From Figure 3.20, $p_u = 8.7 \times \tau_{max} \times D = 6090$ kN/m.
3. From Figures 3.21a and 3.21b, $\alpha = -5.5$ and $m = 0.3500$.

The resulting deflection and rotation at the monopile head are showcased in Figure 3.31. It is evident that the fit of the curves is less successful. Significantly, the positive match achieved for PL3, characterized by a lower L/D ratio and thereby presenting a greater challenge in aligning responses, as illustrated in Figure 3.25, leads to the anticipation of an improved fit for CS. This expectation corresponds with the trends discussed earlier.

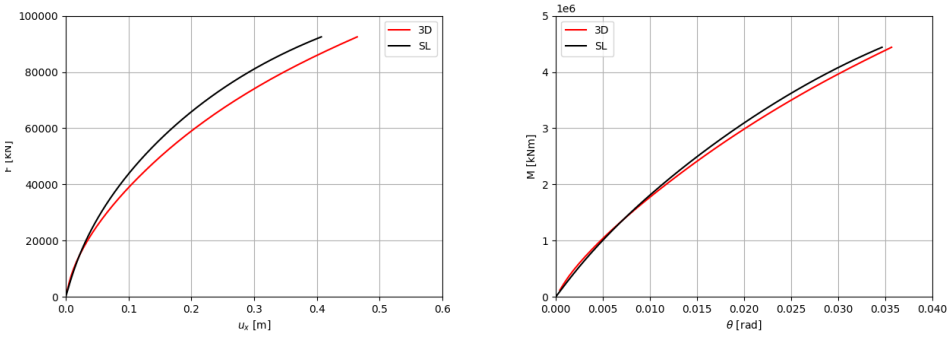

(a) Displacement at mudline.

(b) Rotation at mudline.

Figure 3.31: Global response of monopile CS at mudline: SL material model.

Hence, the alignment depicted for CS in Figure 3.31 seems to be not fully optimized in the current context. This implies that the parameter values obtained for L/D = 5, directly extracted from Figures 3.20 and 3.21, may not be optimal. This observation raises the possibility that the relationship between the optimized values derived for various e/D and L/D ratios might not follow a linear pattern within

the vicinity of L/D = 5. In the subsequent optimization routine, executed within the parameter range limits corresponding to L/D = 4 and L/D = 6 (while presently analyzing L/D = 5), the optimal parameters are successfully determined and the deflection and rotation match at the monopile head is substantially improved, as illustrated in Figure 3.32. It is worth noting that these optimal parameters did not align with the midpoint values, as initially hypothesized. These optimized values are visually represented as data points in blue within Figure 3.33.

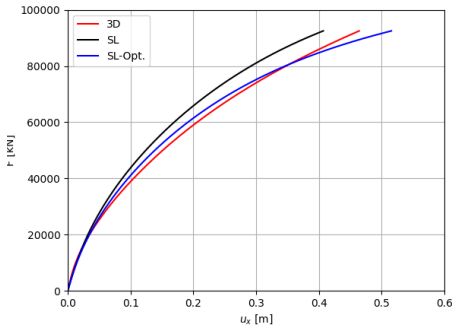

(a) Displacement at mudline.

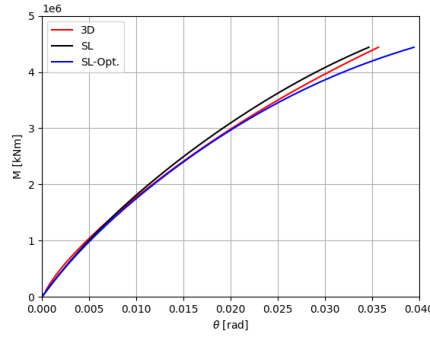

(b) Rotation at mudline.

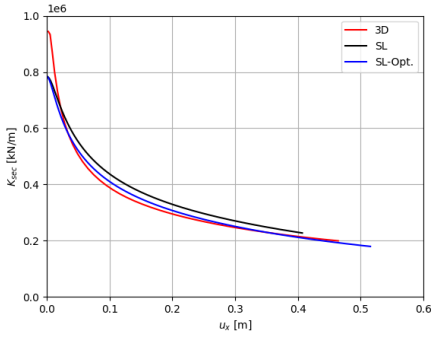

(c) Displacement-based secant stiffness.

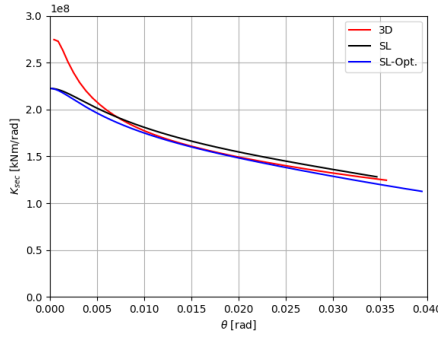

(d) Rotation-based secant stiffness.

Figure 3.32: Global response of monopile CS at mudline: SL material model calibrated based on the suggested step-by-step procedure (black line) and calibrated upon optimisation (blue line).

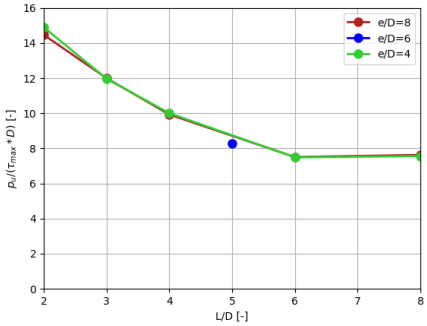

(a) Optimised p_u parameter.

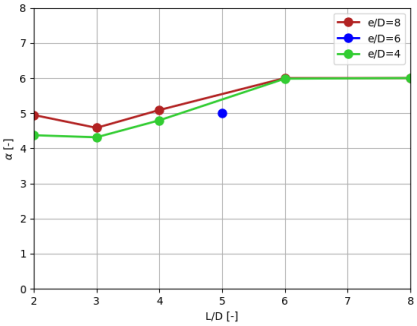

(b) Optimised α parameter.

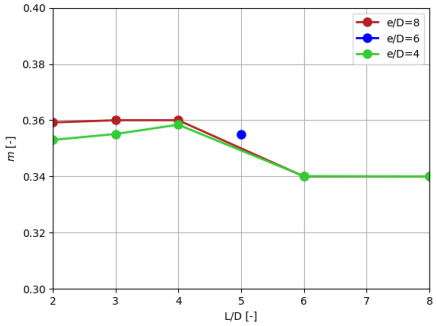

(c) Optimised m parameter.

Figure 3.33: Optimised SL parameters for CS.

Some important points need to be emphasized. Firstly, it's crucial to note that the chosen L/D ratio falls within the region where transitions occur on the graphs. As a result, this particular choice inherently presents a challenging scenario. On a positive note, the optimal solution was successfully located within the anticipated parameter ranges for all three variables. Consequently, it is reasonable to propose conducting additional analyses for a broader range of L/D ratios. By doing so, a greater number of data points can be gathered, enabling the derivation of a more accurate function that effectively models the data. It is important to provide comprehensive insights into the process of parameter selection from the graph. This is

particularly crucial given the demonstrated sensitivity of the parameters, where even the decimal fractions of the dimensionless parameters α and m hold a substantial influence.

Lastly, the distribution of errors for the examined 1D models is depicted in Figure 3.34. When applying the optimized SL parameters, represented as the SL-Opt. curve in the plot, the resulting error distribution aligns with expectations. This closely resembles the error distribution showcased in Figure 3.22. It is worth noting that the accuracy of the SL calibration, achieved through linear interpolation for parameter determination, is not particularly high. In quantitative terms, the error for the SL-Opt. curve stands at approximately 15%, whereas the error for the regular SL curve is around 20%. While this discrepancy might not appear significant, its impact on the fit of monopile head deflection and rotation cannot be disregarded.

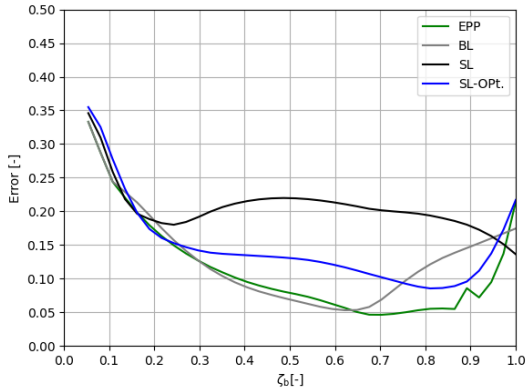

Figure 3.34: Error comparison on CS monopile: EPP, BL, SL material models.

Chapter 4

Conclusions & Recommendations

4.1 Conclusions

The core objective of this master's thesis is to align the response of simplified 1D models with the response of detailed 3D FE models of the soil-monopile system, considering specific assumptions. Initially, the focus is on evaluating the correlation between 1D and 3D results within the framework of linear elastic soil behavior (Chapter 2). This investigation leads to conclusions regarding the degree of alignment with existing literature.

- Validation against analytical solution:
  - Irrespective of load eccentricity, the 1D results obtained from the analyses are validated against the analytical relationships established by Hetényi [19]. This validation process involves adhering to the same fundamental assumptions as prescribed by Hetényi, which encompass the exclusive utilization of lateral shaft springs and the application of the Euler-Bernoulli theory in modelling the pile.
  - The significant shearing contribution to the rotation in low L/D monopiles makes the Euler-Bernoulli theory unsuitable for modeling these piles, consequently rendering Hetényi's analytical solutions, which are based on the Euler-Bernoulli theory, unsuitable for validating the response of these large-diameter monopiles used to support offshore wind turbines.

- Adding up soil reaction components:
  - After evaluating simplified scenarios utilizing constant spring stiffness with depth, as outlined in *Cases 1-4* by Wan et al. [34], several key observations can be made.
    - *Case 4*, employing lateral shaft springs exclusively, yields consistent and validated outcomes, further supported by the findings of Delavinia [10].
    - *Case 3*, incorporating base springs, shows a slight enhancement at the pile tip, yet overall response deteriorates.
    - Conversely, *Case 2*, which includes moment springs with a stiffness equal to unity in addition to the base springs, displays substantial improvement in both deflection and rotation profiles, along with a superior match in monopile head stiffness. Notably, it achieves the most accurate rotation profile alignment among all simplified cases.
    - *Case 1*, which includes all spring mechanisms similar to *Case 2*, but with optimized shaft moment springs, showcases the most accurate deflection profile, but notably underestimates the rotation profile.
    - Both *Cases 1 & 2* present prominent deflection and rotation profiles, distinguished by *Case 1*'s proficiency in deflection and *Case 2*'s proficiency in rotation. Furthermore, *Case 2* achieves the best alignment in terms of lateral and rotational monopile head stiffness.
  - *Case 2 Modified* is an analysis carried out by the author, encompassing all four spring components calibrated similarly to *Case 2*, except for the rotational shaft springs. Notably, the stiffness of the rotational shaft springs is depth-dependent. Thus, each rotational spring along the length of the monopile is individually calibrated. *Case 2 Modified* demonstrates enhanced precision, as evidenced by the nearly identical rotation profile to that of the 3D model. However, the practical application of depth-dependent spring coefficients necessitates complex individual calibration, making this approach impractical for real engineering applications.

In Chapter 3, the focus shifts towards elastoplastic soil modelling, aiming to calibrate the springs of the 1D model to align with the response extracted from the 3D analyses. Prior to delving into the conclusions of this chapter, the key assumptions made are outlined:

- The analyses are conducted under static monotonic loading conditions.

- The 3D analyses adopt an elastic perfectly plastic soil material response.
- In the context of 1D analyses, only lateral shaft springs are utilized.
- For the 1D analyses, the elastic stiffness of the lateral shaft springs undergoes calibration based on *Case 4* of Wan et al. [34]. *Case 4* involves solely translational springs characterized by constant stiffness throughout the depth.
- Scaling the soil stress-strain response to obtain the *p-y* response
  - Scaling procedures are unsuitable for linear elastic perfectly plastic soil modelling due to non-linear *p-y* response caused by variations in soil elements reaching the yield state at different stages. Determining a single yielding point for a match with 3D finite element results is unattainable, revealing a clear dependency between applied force and yielding force, indicative of geometrical (or structural) hardening soil behavior.
- Optimisation process
  The optimization process is initiated to automate the identification of plastic parameters within the 1D spring material response across various monopile geometries and lateral load eccentricities. The RBFOpt (Radial Basis Function Optimization), an open-source Python library, is employed to perform optimisation. The objective function (error) quantified the match in deflection and rotation profiles.
  - The linear elastic perfectly plastic (EPP) model encompasses a single optimization parameter, namely the yielding deformation δ_y. The EPP model cannot be uniquely calibrated to exhibit satisfactory performance across the entire range of loads examined. Hence, the EPP approach is not suitable due to its inherent load-dependent nature, highlighting the necessity for an alternative spring response that is inherently load-independent to address this limitation effectively.
  - The bilinear (BL) spring modelling offers a load-independent solution with two defining variables: the first yielding point (δ_y) and the inclination of the linear hardening branch (K_h). With the appropriate variables in place, the BL modelling yields accurate results that align well with the 3D analysis, ensuring dependable predictions for soil-monopile interaction. Two graphs are provided, each illustrating variable relationship with aspect ratio and load eccentricity, empowering users to select appropriate BL variables.

  - The exponential spring modelling, notably the Suryasentana and Lehane's (SL) *p-y* relationship [29], is utilized. This model is defined by three parameters: p_u (ultimate soil reaction force per unit length), α (dimensionless plastic stiffness parameter), and m (dimensionless curvature parameter). Accompanied by three informative graphs, these variables' correlations with aspect ratio and load eccentricity are depicted, enabling users to make informed choices in selecting suitable SL variables.

- Comparison of the EPP, BL and SL models
  - The error distributions of the EPP and BL models showed similar errors during the initial loading phase, indicating linear soil response and no plasticity at this stage. In contrast, the SL model's initial error distribution diverges due to the challenge of defining a single parameter set that matches early errors and maintains low errors throughout the entire loading range. The selection of optimal parameter values is aimed at achieving consistent responses across the complete load spectrum and has been demonstrated to yield accurate results.
  - More flexible monopiles (higher L/D ratios) demonstrated better alignment with 3D results in terms of deflection and rotation at the monopile head, regardless of whether the spring material followed the BL or SL response. This is attributed to the fact that relying solely on lateral shaft springs yields more precise results for monopiles with higher L/D ratios, where the effects at the base and the developed shaft moment are less prominent.
  - Evident discrepancy observed in rotation-based secant stiffness for low rotations across all piles, due to the the omission of rotational shaft springs in the analysis.
  - Displacement-based secant stiffness for small displacements is accurately represented only for the lower L/D ratio monopiles. This can be attributed to the calibration process, as guided by Wan et al. [34], which was established on an ideally rigid pile. Hence, monopiles with lower L/D ratios exhibit more accurate responses at small displacements due to their relatively stiffer behavior.
  - Overall, BL and SL 1D *p-y* models exhibited agreement with reported 3D response. The SL model is preferred due to its tendency to slightly overestimate deflection and rotation, aligning favorably with safety protocols, unlike the BL model which consistently predicts smaller deflection values compared to 3D simulations.

- Applicability of the proposed empirical design processes for BL and SL *p-y* modelling - Case study evaluation

  - The proposed BL methodology demonstrated satisfactory prediction of deflection and rotation response, validating the applicability of the suggested step-by-step methodology.
  - The SL methodology necessitates local optimization for specific unexamined L/D ratios. However, for the investigated L/D ratios, the SL model demonstrated favorable overall performance.

4.2 Recommendations

Taking into account the findings outlined in the preceding section, the following subjects are proposed for future research:

- Investigation on the applicability of the dimensionless stiffness coefficients as addressed in Wan et al.'s study [34], for the calibration of the elastic spring components for monopiles with L/D ratio greater than 2. Uncertainties regarding the applicability stem from the fact that in Wan et al.'s study [34], a perfectly rigid pile is analysed, which does not find inclusion within the scope of the current master thesis. (Section 2.3)

- Exploration of alternative error formulations for optimization procedures, as demonstrated by other researchers. (Section 3.3.2)

- Adding rotational shaft springs to the 1D analyses to enhance prediction of rotation-based secant stiffness, especially for low rotations. (Section 3.3.3). Additionally, including base springs in the analysis to evaluate their effect on the overall match.

- Evaluation of monopile head stiffness, encompassing all three components of the stiffness matrix, as cited in [5, 3, 28]. (Section 3.3.3)

- Examination of a wider range of L/D and e/D scenarios to elucidate the specific curves of BL and SL model parameters, with a particular focus on the calibration of SL model parameters within the L/D range of 4 to 6. (Section 3.4)

- Analysis of non uniform soil conditions: Further investigation into the behavior of monopiles in non-uniform soil profiles, considering variations in soil properties and layering. Evaluation of the suggested spring stiffness coefficients proposed by Wan et al. [34].
- Analysis under dynamic loading:
  - Evaluation of the damping, both viscous and hysteretic, on the soil-monopile response. Investigation into the inclusion of a dashpot in the 1D spring model setup.
  - Utilization of the extended SL model proposed by Kementzetzidis et al. [21] to address cyclic loading scenarios.

Bibliography

[1] Christelle N. Abadie. *Cyclic Lateral Loading of Monopile Foundations in Cohesionless Soils*. PhD thesis, University of Oxford, 2015.

[2] George Anoyatis, Raffaele Di Laora, Alessandro Mandolini, and George Mylonakis. Kinematic response of single piles for different boundary conditions: Analytical solutions and normalization schemes. *Soil Dynamics and Earthquake Engineering*, 44:183–195, 1 2013.

[3] Laszlo Arany, Subhamoy Bhattacharya, John Macdonald, and Stephen J. Hogan. Design of monopiles for offshore wind turbines in 10 steps. *Soil Dynamics and Earthquake Engineering*, 92:126–152, 1 2017.

[4] Amin Barari, Xiangwu Zeng, Mohammad Rezania, and Lars Bo Ibsen. Three-dimensional modeling of monopiles in sand subjected to lateral loading under static and cyclic conditions. *Geomechanics and Engineering*, 26(2):175–190, 7 2021.

[5] Subhamoy Bhattacharya. *Design of foundations for offshore wind turbines*. John Wiley & Sons, 2019.

[6] Ross W. Boulanger, Christina J. Curras, Bruce L. Kutter, Daniel W. Wilson, and Abbas Abghari. Seismic Soil-Pile-Structure Interaction Experiments and Analyses. *Journal of Geotechnical and Geoenvironmental Engineering*, 125(9):750–759, 9 1999.

[7] Harvey J. Burd, David M.G. Taborda, Lidija Zdravkovic, Christelle N. Abadie, Byron W. Byrne, Guy T. Houlsby, Kenneth G. Gavin, David J.P. Igoe, Richard J. Jardine, Christopher M. Martin, Ross A. McAdam, Antonio M.G. Pedro, and David M. Potts. PISA design model for monopiles for offshore wind turbines: Application to a marine sand. *Geotechnique*, 70(11):1048–1066, 11 2020.

[8] Byron W. Byrne, Guy T. Houlsby, Harvey J. Burd, Kenneth G. Gavin, David J.P. Igoe, Richard J. Jardine, Christopher M. Martin, Ross A. McAdam, David M. Potts, David M.G. Taborda, and Lidija Zdravkovic. PISA design model for monopiles for offshore wind turbines: Application to a stiff glacial clay till. *Geotechnique*, 70(11):1030–1047, 11 2020.

[9] Guangwei Cao, Xuanming Ding, Maoyi Liu, Huan Liu, and Qian Long. Study on Failure Mechanism and Soil Resistance for Laterally-Loaded Large-Diameter Monopiles. *Geotechnical and Geological Engineering*, 6 2023.

[10] Dimitra Delavinia. Seismic response of monopile foundations for offshore wind turbines: from 3D to 1D modelling of soil-foundation interaction. Technical report, Delft University of Technology, 2022.

[11] Dimitra Delavinia, Evangelos Kementzetzidis, Stavros Panagoulias, Apostolos Tsouvalas, and Federico Pisanò. Seismic Soil-monopile-structure Interaction for Offshore Wind Turbines: From 3D to 1D Modelling. In *Offshore Site Investigation Geotechnics 9th Int. Conf. London, United Kingdom*, 2023.

[12] Claudio G. Di Prisco, Manuel Pastor, and Federico Pisanò. Shear wave propagation along infinite slopes: A theoretically based numerical study. *International Journal for Numerical and Analytical Methods in Geomechanics*, 36(5):619–642, 4 2012.

[13] Claudio G. Di Prisco and Federico Pisanò. An exercise on slope stability and perfect elastoplasticity. *Geotechnique*, 61(11):923–934, 2011.

[14] DNV. Energy Transition Outlook 2022. Technical report, Høvik, Norway, 2022.

[15] Alexander I. J. Forrester, András Sobester, and Andy Keane. *Engineering Design via Surrogate Modelling: A Practical Guide*. Wiley J., Chichester, UK, 2008.

[16] George Gazetas and Ricardo Dobry. Simple radiation damping model for piles and footings. *J. Eng. Mech.*, 110(6):937–956, 1984.

[17] Nikos Gerolymos and George Gazetas. Winkler model for lateral response of rigid caisson foundations in linear soil. *Soil Dynamics and Earthquake Engineering*, 26(5):347–361, 5 2006.

[18] Bipin K. Gupta and Dipanjan Basu. Applicability of Timoshenko, Euler-Bernoulli and rigid beam theories in analysis of laterally loaded monopiles and piles. *Geotechnique*, 68(9):772–785, 9 2018.

[19] Miklós Hetényi. Beams on Elastic Foundation: Theory with Applications in the Fields of Civil and Mechanical Engineering. *Univ. of Michigan Press*, 1955.

[20] Philippe Jeanjean, Youhu Zhang, Arash Zakeri, Knut Andersen, Robert Gilbert, and Asitha Senanayake. *A Framework for Monotonic P-Y Curves in Clays*. Society for Underwater Technology, 2017.

[21] Evangelos Kementzetzidis, Federico Pisanò, and Andrei V. Metrikine. A memory-enhanced p-y model for piles in sand accounting for cyclic ratcheting and gapping effects. *Computers and Geotechnics*, 148, 8 2022.

[22] Jinchi Lu, Ahmed Elgamal, and Zhaohui Yang. OpenSeesPL: 3D Lateral Pile-Ground Interaction User Manual (Beta 1.0). Technical report, 2011.

[23] Giacomo Nannicini. RBFOpt user manual. Technical report, IBM T. J. Watson, Yorktown Heights, NY., 2021.

[24] Amin Rahmani, Mahdi Taiebat, Liam Finn, and Carlos Ventura. Determination of Dynamic p-y Curves for Pile Foundations Under Seismic Loading. Lisbon, Portugal, 2012. Fifteenth World Conference on Earthquake Engineering.

[25] Amin Rahmani, Mahdi Taiebat, Liam Finn, and Carlos Ventura. Evaluation of p-y springs for nonlinear static and seismic soil-pile interaction analysis under lateral loading. *Soil Dynamics and Earthquake Engineering*, 115:438–447, 12 2018.

[26] Lymon C. Reese, William R. Cox, and Francis D Koop. Analysis of laterally loaded piles in sand. In *OTC Offshore Technology Conference*, 1974.

[27] Sergio Sánchez, José Santos López-Gutiérrez, Vicente Negro, and M. Dolores Esteban. Foundations in offshore wind farms: Evolution, characteristics and range of use. Analysis of main dimensional parameters in monopile foundations, 12 2019.

[28] Masoud Shadlou and Subhamoy Bhattacharya. Dynamic stiffness of monopiles supporting offshore wind turbine generators. *Soil Dynamics and Earthquake Engineering*, 88:15–32, 9 2016.

[29] Stephen K. Suryasentana and Barry M. Lehane. Updated CPT-based p–y formulation for laterally loaded piles in cohesionless soil under static loading. *Geotechnique*, 66(6):445–453, 6 2016.

[30] William F. Van Impe and Shin Tower Wang. The advanced p-y method for analyzing the behaviour of large-diameter monopiles supporting offshore wind turbines. In *E3S Web of Conferences*, volume 205. EDP Sciences, 11 2020.

[31] Willem G. Versteijlen. *Identification of effective 1D soil models for large-diameter offshore wind turbine foundations based on in-situ seismic measurements and 3D modelling*. PhD thesis, 2018.

[32] Willem G. Versteijlen, João De Oliveira Barbosa, Karel N. Van Dalen, and Andrei V Metrikine. Method for extracting an equivalent Winkler model of the 3D dynamic soil-structure interaction of large-diameter offshore monopile foundations. In *Proceedings of XLIII International Summer SchoolConference APM 2015*, pages 436–447, 2015.

[33] Willem G. Versteijlen, Andrei V. Metrikine, and Karel N. van Dalen. A method for identification of an effective Winkler foundation for large-diameter offshore wind turbine support structures based on in-situ measured small-strain soil response and 3D modelling. *Engineering Structures*, 124:221–236, 10 2016.

[34] Xiao Wan, James P. Doherty, and Mark F. Randolph. Relationships between lateral and rotational load transfer stiffnesses and soil modulus for the elastic response of monopiles. *Computers and Geotechnics*, 137, 9 2021.

[35] Shaomin Wang, Bruce L. Kutter, Jacob M. Chacko, Daniel W. Wilson, Ross W. Boulanger, and Abbas Abghari. Non linear seismic soil pile structure interaction. *Earthquake Spectra*, 14(2):377–396, 1998.

[36] Wind Europe. Wind energy in Europe in 2019 - trends and statistics. Technical report, Wind Europe, Brussels, Belgium, 2020.

[37] Xiaodi Zhang, Baojian Li, Zhongxuan Yang, Bitang Zhu, Rongqiao Xu, J. C. Wang, and Xiaonan Gong. Timoshenko beam theory–based analytical solution of laterally loaded large-diameter monopiles. *Computers and Geotechnics*, 161, 9 2023.

[38] Youhu Zhang and Knut H. Andersen. Scaling of lateral pile p-y response in clay from laboratory stress-strain curves. *Marine Structures*, 53:124–135, 5 2017.

Appendix A

Further Results

A.1 Comparison of the 1D BL and SL Models for PL1*, PL3* and PL5*

The analysis, as highlighted in Section 3.3.3, provides valuable insights into the alignment between 1D and 3D *p-y* modeling, regardless of the chosen e/D ratio. Specifically, Section 3.3.3 presented results for e/D equal to 8, while this section focuses on the same pile geometries but with e/D equal to 4, depicted in Figures A.1, A.2, and A.3.

The modeling accuracy is highest for the more 'flexible' pile and gradually diminishes as we examine the behavior of the more 'rigid' pile. However, when it comes to accurately capturing the initial displacement-based secant stiffness, the most 'rigid' pile outperforms the others. Nevertheless, challenges arise in accurately representing rotation-based secant stiffness, particularly for minor rotations, across all examined geometries.

Lastly, it is noteworthy that the SL model tends to overestimate both deflection and rotation at the monopile head. While this might seem like a drawback, this conservative approach aligns well with engineering safety practices, placing the SL model in an advantageous position.

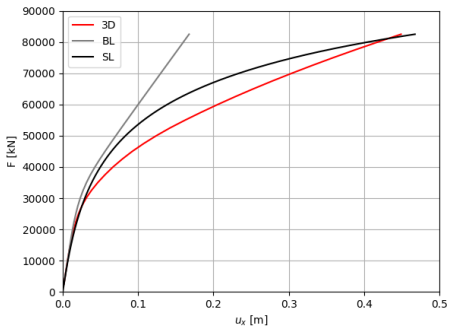

(a) Displacement at mudline.

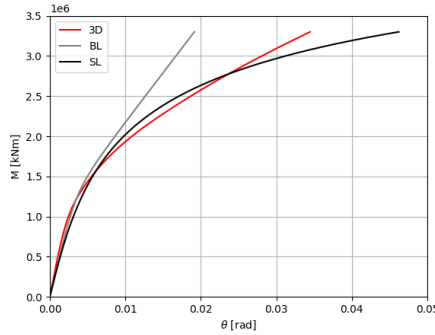

(b) Rotation at mudline.

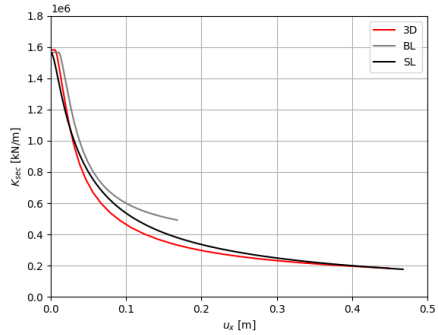

(c) Displacement-based secant stiffness.

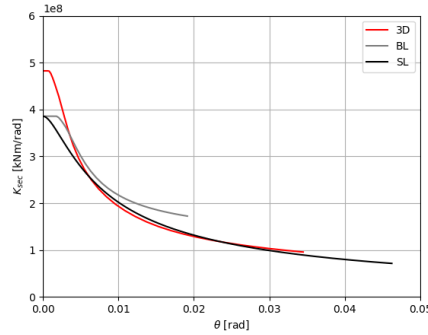

(d) Rotation-based secant stiffness.

Figure A.1: Global response of monopile PL1* at mudline.

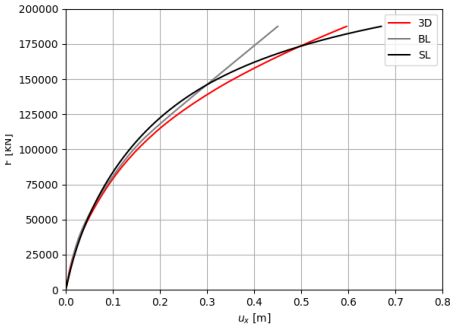

(a) Displacement at mudline.

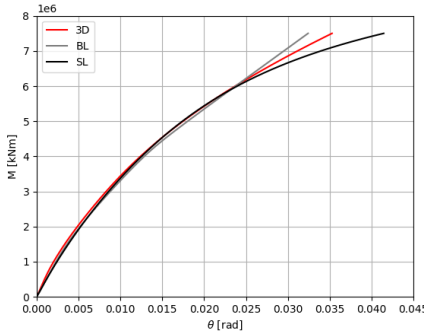

(b) Rotation at mudline.

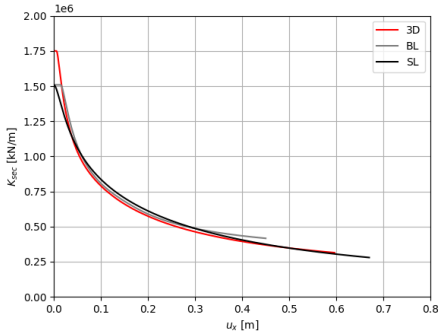

(c) Displacement-based secant stiffness.

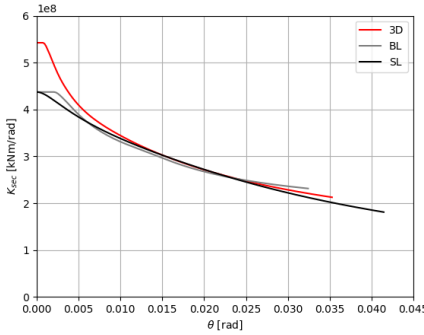

(d) Rotation-based secant stiffness.

Figure A.2: Global response of monopile PL3* at mudline.

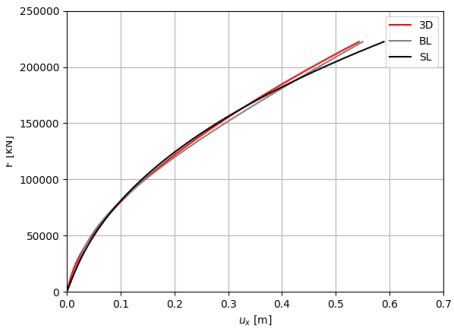

(a) Displacement at mudline.

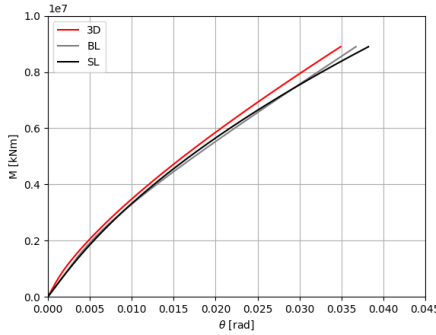

(b) Rotation at mudline.

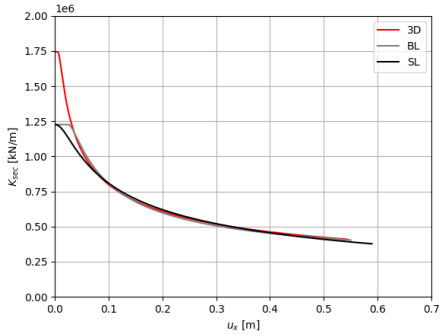

(c) Displacement-based secant stiffness.

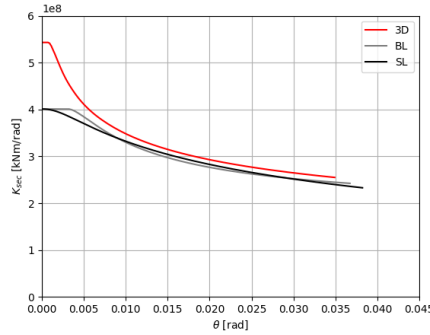

(d) Rotation-based secant stiffness.

Figure A.3: Global response of monopile PL5* at mudline.

TU Delft Delft University of Technology

SIEMENS Gamesa RENEWABLE ENERGY